Non-Collinear Second Harmonic Generation in Strontium Barium Niobate

Dissertation zur Erlangung des Grades
Doktor der Naturwissenschaften

von
Arthur R. Tunyagi

vorgelegt dem Fachbereich Physik der

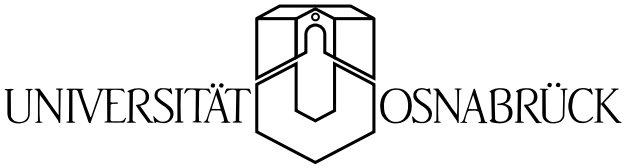

im September 2004

Contents

Chapter 1

Introduction

An increasing number of photonic applications based on nonlinear effects are routinely in use, but for other desired and in principle possible new commercial devices, light induced nonlinear effects are too small. For known materials the time constants, their long-term stability or other properties are not sufficient and thus often the demands of light intensity or power are too high. Thus the field of nonlinear interactions is still in rapid progress and new applications with strong economic and social implications can be expected.

In the current work we focused on studying the ferroelectric Tungsten-Bronze structure Strontium-Barium-Niobate (SBN) crystal. Many interesting properties of this material were earlier reported in the literature [1–6]. Nevertheless a new effect -we called it domain-induced-second-harmonic-generation (DISHG) [7]- was discovered, which not only explains the mechanism of the second harmonic generation in this material but also extends the potential nonlinear-optical applications of SBN.
Using the particularities of the second harmonic generation in this material, cylindrically polarized light can be obtained in a very easy manner. It was shown in the literature [8–12] that due to its high symmetry light with this polarization state can be better focused than in all other cases. Up to now this is the easiest way to obtain such a polarization state, thus a patent was applied for in this direction [13]. Several devices where the focusing quality of the light is of great importance like in the case of confocal microscopy or optical memory devices represents potential applications.
Beside the potential new applications the DISHG opens the possibility to investigate important characteristics of the ferroelectric domains of the SBN crystal.

Beside the introduction section where this overview of the work is presented there are six more chapters in the structure of the thesis.
The second chapter describes the SBN crystal. The structure is presented and several properties, important for this work, are shown.
In the third chapter an introduction in the field of nonlinear optics is made. All known SHG mechanisms are briefly summarized and all their requirements are pointed out. The importance of the refractive index in the phase-matching process is shown.

The next chapter presents measurements of the refractive index for the whole composition range and from infrared to near ultraviolet. As results of the measurements one can conclude that no known SHG scheme can be held responsible for the harmonic generation in the case of the SBN crystal.
The fifth chapter presents observations of the SHG experiments. The observed light patterns strongly indicate that some phase-matching process must be considered even if the refractive index measurements and the known SHG schemes could not explain it. Further, in the same chapter, a new mechanism to explain the observations is presented. The needle-like domain structure of the crystal is considered to play an active role in the second harmonic process. Thus the new mechanism is called domain-induced-second-harmonic-generation (DISHG). Results of two experiments confirming the new model are presented. This chapter ends with a brief description of the focusing of the cylindrically polarized light and a description of potential application.
Chapter number six presents applications of the DISHG made to determine characteristics of the crystal. From the inflection point of the second-order nonlinear susceptibility as function of temperature the ferroelectric-paraelectric phase transition temperature is determined. Size-characteristics of the ferroelectric domains are further investigated. The development of the crystal domains from the as-grown to electrically-poled state is analyzed. Particular aspects of the relaxor phase transition of the SBN crystal are also investigated using DISHG.
The last chapter summarizes all important results of the work.

Chapter 2

Structure of the Strontium-Barium-Niobium Crystal

2.1 Introduction

Due to its outstanding photorefractive, electrooptic, nonlinear optic and dielectric properties, strontium barium niobate, $Sr_xBa_{1-x}Nb_2O_6$ -henceforth denoted as SBN, is one of the most interesting materials in these fields. Potential applications include pyroelectric detection [1], holographic data storage [2], surface acoustic wave devices [14], phase conjugation [15], generation of photorefractive solitons [16], quasi-phase-matching second-harmonic generation [17] and electro-optic modulation [18]. These materials belong to the extensively studied class of relaxor ferroelectrics [19,20] for which the characteristics of the ferroelectric phase transition (its smearing and temperature) and, hence, all the parameters are governed by the composition, i.e. the [Sr]/[Ba] ratio.

2.2 SBN Growth and Structure

The SBN crystals are grown by the Czochralski method. For this work all crystals were grown in the crystal growth laboratory of the Osnabrück University. As growth parameters one can mention that the vertical temperature gradient in the furnace was about 1°C/cm. The seed crystal was air-cooled and continuously rotated with 28 cycles per minute. The crystals are grown in the c-direction and pulled-out with a speed of 0.4 to 0.8 mm/h. The obtained crystals were around 5 mm in width and up to 10 cm in length [21].

The structure of the SBN crystals was investigated in a number of works [3–6]. Figure 2.1 shows the projection of the SBN structure onto the (c)-plane, which was proposed by Jamieson et al. [3]. The SBN structure is build up of two types of crystallographically independent NbO_6 octahedra joined via oxygen corners into a three-dimensional network. As follows from all the structural investigations [3–6], in the SBN structure the narrowest channels with a triangle cross-section (channels C in Fig. 2.1 and Fig. 2.2) are empty, the

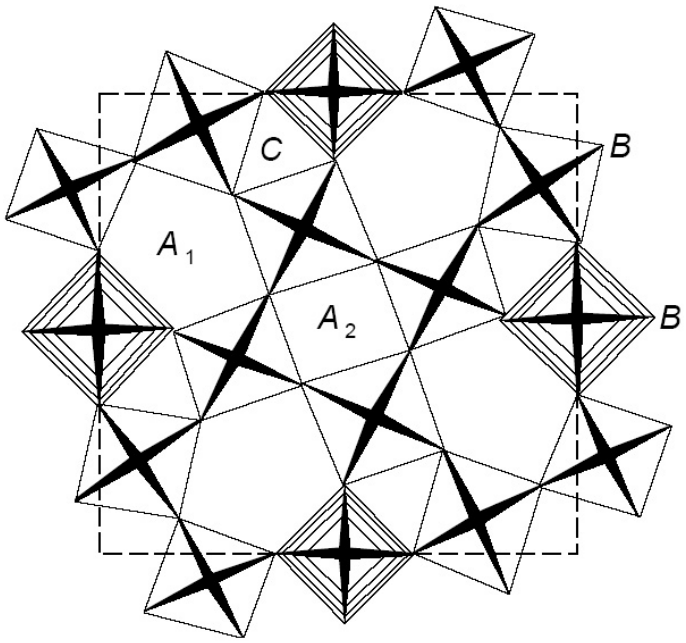

Figure 2.1: Projection of the (Sr,Ba)Nb_2O_6 structure onto the (c)-plane. One can see the two types of NbO_6 octahedra denoted with B. The narrowest triangle cross-section channels are denoted with C. The intermediate diameter tetragonal cross-section channels are labelled with A2. The largest diameter pentagonal channels are marked with A1.

tetragonal channels A2 with an intermediate diameter are occupied only by the Sr atoms, and the largest channels A1 with a pentagonal cross-section are filled by Ba and Sr atoms.

According to the phase diagram [21] and the data obtained in [3–6], the SBN crystals of the structural type under consideration exist in the composition region $Sr_{0.32}Ba_{0.68}Nb_2O_6$ to $Sr_{0.82}Ba_{0.18}Nb_2O_6$ and show a tetragonal symmetry with the space group $P4bm$ and belong to the Tungsten-Bronze (TB) group. The pioneering work by Jamieson et al. [3] was devoted to the structural analysis of the $Sr_{0.75}Ba_{0.25}Nb_2O_6$ compound. It was demonstrated that the Ba atoms located only in the large channels occupy their own fourfold site with an occupancy factor of 34.4%. The same sites are 50.3% filled by Sr atoms. Therefore, each of these crystallographic sites is randomly occupied by the Ba and Sr atoms with a total occupancy factor of 84.7%. The remaining Sr atoms occupy twofold sites in the tetragonal channels with an occupancy of 82.2%. For different [Sr]/[Ba] ratio the occupancy of the channels will change. In the case of the congruently melting composition $x = 0.61$ the medium-size channels are occupied 72.5% by the Sr atoms. The rest of the Sr atoms and Ba atoms occupy the large five-fold channels.
One can see that none of the channels at none of the compositions is completely filled. Thus the structure is called *unfilled* and several properties of the material are influenced

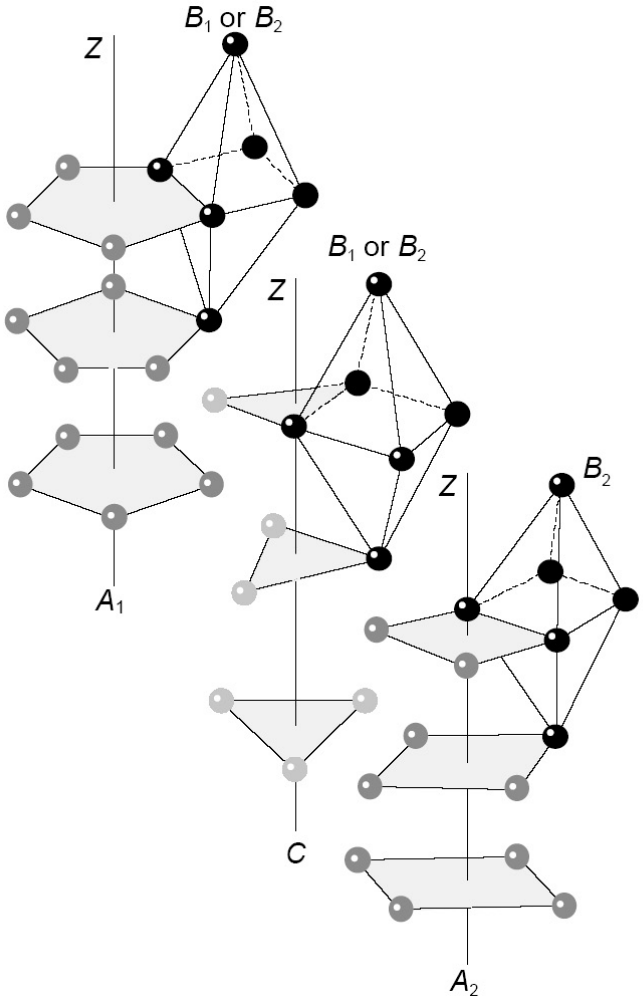

Figure 2.2: Detailed view of the structural-channels in the SBN crystal. The narrowest triangle cross-section channels are denoted with C. The intermediate diameter tetragonal cross-section channels are labelled with A2. The largest diameter pentagonal channels are marked with A1.

by this fact [22, 23]. X-ray diffraction measurements [24] revealed the tetragonal structure of the material *P4bm*. The unit cell parameters vary almost linearly with composition (Dissertation M. Ulex), a = 12.488 to 12.412 Å and c = 3.974 to 3.905 Å for x = 0.32 to 0.82.
At room temperature the crystal is in a ferroelectric phase with the point group 4 m m. At higher temperature, depending on the [Sr]/[Ba] ratio, a ferroelectric-paraelectric phase transition will bring the crystal into a centrosymmetric phase characterized by the point group 4/m m m. Due to the fact that both phases of the crystal are tetragonal the ferroelectric domains in this material are always parallel or antiparallel to the fourfold

axes (180° domains).

2.3 Limitations

Certain properties of the SBN crystal limit its applicability in some fields of optics or nonlinear-optics. The investigation of the optical quality of the crystal, done with an optical microscope, revealed some typical patterns classified as stress in the crystal. In Fig. 2.3 a microscopic picture of the (c)-plane of an SBN crystal between crossed polarizers is presented. The pattern seen in this image seems to come from the stress in the material imposed during its growth. Different parameters of the growth-process could not eliminate this unwanted feature. It must be mentioned that this striations are present only in the non-congruent compositions. The congruently melting composition can be grown with a high optical quality.

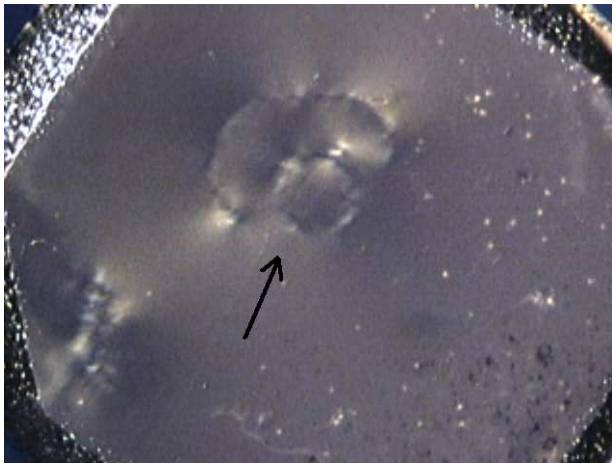

Figure 2.3: Microscopic image of the (c)-plane of an SBN:45 crystal between crossed polarizes.

SBN is part of the large family of Tungsten-Bronze ferroelectric crystals. In the entire class its birefringence is one of the smallest. The direct consequence of this is the impossibility of collinear phase-matched second harmonic generation. Thus efficient frequency-doubling of an infrared laser is not possible with this material. Nevertheless its particular needle-like domain structure enables second harmonic generation in this material which represents a potential for a new sort of applications [7].
The irreproducibility of several properties of the crystal, like the electrical conductivity which can vary in a large spectrum for the same composition from one growth to another represent another limitation of this material. Doping the crystal with rare-earth elements may be a solution for this problem. Thus many studies of doped SBN have been made and many are still in progress.

Even so, with this limitations the SBN crystal is one of the most important and widely investigated member of all Tungsten-Bronze ferroelectric compounds.

Chapter 3

Optical Nonlinearities and Harmonic Generation

> "Physics would be dull and life most unfulfilling if all physical phenomena around us were linear. Fortunately, we are living in a nonlinear world. While linearization beautifies physics, nonlinearity provides excitement in physics."
>
> Y.R.Shen in *The Principles of Nonlinear Optics*

3.1 Optical Nonlinearities

Nonlinear effects in optics offer the possibility of generating or manipulating light in almost any manner. The laser itself, producing light not available in nature, is the most obvious example.
Because of the extremely small photon-photon interaction cross-section the direct influence of one light beam on another is not practical with today's light sources. Therefore the nonlinearity is achieved via the nonlinear interaction of light with matter. In comparison to linear optics both the real and the imaginary part of the refractive index, or in other words both the conventional refractive index n and the absorption coefficient α become functions of the light intensity I or more precise of the electric field $E(r,t)$

$$n = f\{I, \lambda, \phi\} = f\{E(r,t), \lambda, \phi\} \tag{3.1}$$

$$\alpha = f\{I, \lambda, \phi\} = f\{E(r,t), \lambda, \phi\} \tag{3.2}$$

and thus they become functions of space, wavelength, time and polarization, dependent on the incident light.

Matter	Light	Useful description
Nonresonant (transparent)	Incoherent	Maxwell's equations
Nonresonant (transparent)	Coherent	Maxwell's equations
Resonant (absorbing)	Incoherent	Rate equations
Resonant (absorbing)	Coherent	Density matrix formalism

Table 3.1: Types of nonlinear optical interactions of light with matter

Therefore in nonlinear optics the light has to be characterized very carefully to avoid unwanted side effects in applications and to exclude measurement errors, e.g. in nonlinear spectroscopy. The superposition of light in matter will produce new physical effects in the nonlinear regime. All the properties of the newly generated light can be completely different from the properties of the incident beam.
An increasing number of photonic applications based on these nonlinear effects are routinely in use, but for other desired and in principle possible new commercial devices, light induced nonlinear effects are too small. For known materials the time constants, their long-term stability or other properties are not sufficient and thus often the demands of light intensity or power are too high. Thus the field of nonlinear interactions is still in rapid progress and new applications with strong economic and social implications can be expected.

3.1.1 General Classification

There are three useful approaches to the description of the nonlinear interaction of light with matter or more precisely for the *nonlinear modification of matter* by light. One can use Maxwell's equation as the fundamental concept with the nonlinear polarization P_{nl}; the second is based on a quantum mechanical density matrix formalism; and the third neglects the coherent terms in the density matrices and results in rate equations for the population density N_i (Table 3.1).
The first approach is especially useful for nonresonant (elastic) interaction in which the light is not absorbed by the matter. The density matrix is useful for resonant, coherent interaction. In this case the discrete structure of the energy levels of the matter and their phase-dependent occupation during the light wave period may be important for an exact description. Unfortunately this formalism does not allow the description of systems with many energy levels. In this case the description with rate equations may be a useful tool for the analysis of the nonlinear resonant interactions.
The incoherent nonresonant interaction occurs e.g. in the self-focusing of light and coherent nonresonant interactions are e.g. used for frequency conversion. Resonant interaction, which mean absorption or emission of the light in material, is achieved incoherently in nonlinear spectroscopy and applications such as e.g. passive Q-switching. Resonant coherent interaction, in which the matter oscillates in phase with the light, takes place in very fast or high intensity or coherent experiments, as, e.g. self induced transparency. Besides these

extreme cases all kinds of mixed interactions are possible.

3.1.2 Nonresonant Interactions

Nonresonant interactions are most useful for e.g. wavelength conversion of laser light, wave mixing and optical phase conjugation. Because of the negligible absorption almost no energy will be stored in the material. Thus they can be applied for high average powers with high efficiencies.
The nonresonant nonlinear interaction may be understood as the reaction of the electric dipoles built by electrons and the positively charged atomic cores in the matter under the influence of high electric fields. For small fields the elongation will be small and thus the back driving force will change linearly with the elongation in this first order approach, as in classical mechanics. With strong electric fields the elongation will be increased and the force will become a nonlinear function of the elongation.
With conventional light sources the electric fields are in the range of 100 V/m and the resulting elongation is smaller than 10^{-16} m which is small compared to atomic or molecular diameter of $10^{-10}...10^{-7}$ m. With laser radiation electric field values of more than 10^6 V/m can be achieved and thus nonlinear effects are possible.
These nonlinear effects will be a function of the electric fields of the incident light with increasing exponent starting with 1 for linear interactions, to 2 as the next approximation and so on. For better understanding the resulting effects can be classified for this exponent of the nonlinearity as a function of the incident field as follows:

Second-Order Effects

- sum and difference frequency generation
- second harmonic generation (SHG)
- optical parametric amplification (OPA, OPO)
- Pockels effect
- electro-optic beam deflection
- optical rectification

Third-Order Effects

- third harmonic generation (THG)
- Kerr effect
- self-focusing
- self-diffraction

- self-phase modulation
- solitons
- four-wave mixing (FWM)
- optical phase conjugation (PC)

Higher-Order Effects

- high harmonic generation

All these effects are based on the nonlinear modulation of the dielectric constant of the material by the incident light as a result of the strong forces from the interaction of the electric light field vector with the electrons of the matter. These forces drive the electrons out of the harmonic potential and generate anharmonic effects. Mixed cases and noninteger exponents are possible.

3.1.3 Nonlinear Polarization of the Medium

Based on Maxwell's equations the reaction of matter under the influence of the electric field of the light $\mathbf{E}(\mathbf{r}', t')$ can be described by the polarization $\mathbf{P}(\mathbf{r}, t)$. The linear interaction is described as the proportional increase of the polarization as a function of the electric field amplitude [25–28]

$$\mathbf{P}(\mathbf{r}, t) = \varepsilon_0 \int_{-\infty}^{\infty} \chi^{(1)}(\mathbf{r} - \mathbf{r}', t - t') \cdot \mathbf{E}(\mathbf{r}', t') d\mathbf{r}' dt' \tag{3.3}$$

where $\chi^{(1)}$ is the linear susceptibility of the medium. Usually monochromatic plane waves are assumed, $\mathbf{E}(\mathbf{k}, \omega) = E_0(\mathbf{k}, \omega) exp(i\mathbf{k} \cdot \mathbf{r} - i\omega t)$, then a Fourier transformation applied to Eq. 3.3 yields

$$\mathbf{P}(\mathbf{k}, \omega) = \varepsilon_0 \chi^{(1)}(\mathbf{k}, \omega) \mathbf{E}(\mathbf{k}, \omega) \tag{3.4}$$

with

$$\chi^{(1)}(\mathbf{k}, \omega) = \int_{-\infty}^{\infty} \chi^{(1)}(\mathbf{r}, t) exp(-i\mathbf{k}\mathbf{r} + i\omega t) d\mathbf{r} dt \tag{3.5}$$

The dependence of χ on $\mathbf{k}$ is only weak, in nearly all practical cases it can be neglected. In the nonlinear case, $\mathbf{P}$ can be expanded into a power series of $\mathbf{E}$

$$\begin{aligned}
\mathbf{P}(\mathbf{r},t) &= \varepsilon_0 \int_{-\infty}^{\infty} \chi^{(1)}(\mathbf{r}-\mathbf{r}',t-t')\cdot\mathbf{E}(\mathbf{r}',t')d\mathbf{r}'dt' \\
&+ \varepsilon_0 \int_{-\infty}^{\infty} \chi^{(2)}(\mathbf{r}-\mathbf{r}_1,t-t_1;\mathbf{r}-\mathbf{r}_2,t-t_2)\cdot\mathbf{E}(\mathbf{r}_1,t_1)\cdot\mathbf{E}(\mathbf{r}_2,t_2)d\mathbf{r}_1dt_1d\mathbf{r}_2dt_2 \\
&+ \varepsilon_0 \int_{-\infty}^{\infty} \chi^{(3)}(\mathbf{r}-\mathbf{r}_1,t-t_1;\mathbf{r}-\mathbf{r}_2,t-t_2;\mathbf{r}-\mathbf{r}_3,t-t_3)\cdot\mathbf{E}(\mathbf{r}_1,t_1)\cdot \\
&\quad \mathbf{E}(\mathbf{r}_2,t_2)\cdot\mathbf{E}(\mathbf{r}_3,t_3)d\mathbf{r}_1dt_1d\mathbf{r}_2dt_2d\mathbf{r}_3dt_3 \\
&+ \ ...
\end{aligned} \tag{3.6}$$

where $\chi^{(n)}$ is the nth-order nonlinear susceptibility. As in the linear case, the problem can be Fourier transformed. Yet, for $\mathbf{E}$ now a sum of monochromatic plane waves should be assumed

$$\mathbf{E}(\mathbf{r},t) = \sum_i \mathbf{E}(\mathbf{k}_i,\omega_i) \tag{3.7}$$

yielding for the polarization

$$\mathbf{P}(\mathbf{k},\omega) = \mathbf{P}^{(1)}(\mathbf{k},\omega) + \mathbf{P}^{(2)}(\mathbf{k},\omega) + \mathbf{P}^{(3)}(\mathbf{k},\omega) + ... \tag{3.8}$$

with

$$\begin{aligned}
\mathbf{P}^{(1)}(\mathbf{k},\omega) &= \varepsilon_0\chi^{(1)}(\mathbf{k},\omega)\cdot\mathbf{E}(\mathbf{k},\omega) \\
\mathbf{P}^{(2)}(\mathbf{k},\omega) &= \varepsilon_0\chi^{(2)}(\mathbf{k}=\mathbf{k}_i+\mathbf{k}_j,\omega=\omega_i+\omega_j)\cdot\mathbf{E}(\mathbf{k}_i,\omega_i)\cdot\mathbf{E}(\mathbf{k}_j,\omega_j) \\
\mathbf{P}^{(3)}(\mathbf{k},\omega) &= \varepsilon_0\chi^{(3)}(\mathbf{k}=\mathbf{k}_i+\mathbf{k}_j+\mathbf{k}_l,\omega=\omega_i+\omega_j+\omega_l)\cdot\mathbf{E}(\mathbf{k}_i,\omega_i)\cdot \\
&\quad \cdot\mathbf{E}(\mathbf{k}_j,\omega_j)\cdot\mathbf{E}(\mathbf{k}_l,\omega_l)
\end{aligned} \tag{3.9}$$

The $\chi^{(n)}(\mathbf{k},\omega)$ can be expressed in a similar way as in the linear case as integrals over the respective $\chi^{(n)}(\mathbf{r},t)$. Again, the dependence on $\mathbf{k}$ can be neglected. $\chi^{(n)}$ is an $(n+1)$ - rank tensor representing material properties. Using Einstein's summation convention, the above equations may be rewritten in component form, e. g.

$$P_k^{(2)}(\omega) = \varepsilon_0\chi_{kmn}^{(2)}(\omega=\omega_i+\omega_j)E_m(\omega_i)E_n(\omega_j) \tag{3.10}$$

3.1.4 The *Phase Matching* Problem

The fundamental waves generate an oscillating polarization through the medium which oscillates with ω. The phases at different locations are defined and connected by the fundamental waves travelling through the medium. That means that the polarization wave travels through the medium at a velocity $v(\omega_i,\omega_j)$ for the fundamental frequencies ω_i,ω_j .

The local polarization at every location acts as a source of electromagnetic dipole radiation. The generated free waves, yet, travel through the medium at a velocity $v(\omega)$ characteristic for their own frequency ω.

The velocities are defined by the respective refractive indices and - due to the dispersion present in all materials - generally are different. In an extended medium the two relevant waves - polarization wave and generated free wave - thus come out of phase after a typical distance commonly referred to as coherence length. The sum free wave is amplified due to constructive interference up to this coherence length, then attenuated due to destructive interference. No efficient generation of nonlinear radiation seems to be possible. Yet, there are some solutions to the problem.

3.1.5 Structural Symmetry of Nonlinear Susceptibilities

The susceptibility tensors must remain unchanged upon symmetry operations allowed for the medium. This reduces the number of independent and nonzero elements. The most important conclusion from this property is that for all centrosymmetric crystals and for all isotropic media (gases, liquids, amorphous solids) all tensor elements of the even-order susceptibility tensors ($\chi^{(2)}, \chi^{(4)}, ...$) must be zero. Thus, e. g., no second harmonic generation can be observed in such media. Odd-order susceptibility tensors, yet, will be non-zero and will provide nonlinear effects. Using gases or metal vapors, e. g., only odd-order harmonics can be produced.

3.1.6 Permutation Symmetry of Nonlinear Susceptibilities

When tensors are multiplied with vectors, usually the order of the vector multiplication can be changed. In nonlinear optics it should not matter which of the fundamental fields is the first to be multiplied. From this, permutation symmetry for the nonlinear susceptibilities follows, for the second order

$$\chi^{(2)}_{ijl}(\omega_1, \omega_2) = \chi^{(2)}_{ilj}(\omega_2, \omega_1) \tag{3.11}$$

Besides this trivial one, a more general permutation symmetry can be defined due to time reversal symmetry resulting in relations like

$$\chi^{(2)*}_{ijl}(\omega = \omega_1 + \omega_2) = \chi^{(2)}_{jli}(\omega_1 = -\omega_2 + \omega) = \chi^{(2)}_{lij}(\omega_2 = \omega - \omega_1) \tag{3.12}$$

Time reversal symmetry can be applied as long as absorption can be neglected.

If the dispersion of χ can also be neglected, then the permutation symmetry becomes independent of the frequencies. Consequently, then a very general permutation symmetry exists between different elements of χ: elements remain unchanged under *all* permutations of the Cartesian indices. This so-called *Kleinman's conjecture or Kleinman symmetry* [29]

reduces the number of independent elements further. Yet, it should be noted that it's a good approximation only at frequencies far from resonances such that dispersion really can be neglected.

3.1.7 Symmetry in the case of Strontium Barium Niobate

In the ferroelectric phase at room temperature Strontium Barium Niobate has the point symmetry group 4mm. The symmetry operations present in the point group include

$$\begin{aligned} 4: &\begin{pmatrix} x \to y \\ y \to -x \\ z \to z \end{pmatrix} \begin{pmatrix} x \to -x \\ y \to -y \\ z \to z \end{pmatrix} \begin{pmatrix} x \to -y \\ y \to x \\ z \to z \end{pmatrix} \\ m: &\begin{pmatrix} x \to -x \\ y \to y \\ z \to z \end{pmatrix} \begin{pmatrix} x \to x \\ y \to -y \\ z \to z \end{pmatrix} \\ m: &\begin{pmatrix} x \to y \\ y \to x \\ z \to z \end{pmatrix} \begin{pmatrix} x \to -y \\ y \to -x \\ z \to z \end{pmatrix} \end{aligned} \tag{3.13}$$

The tensor elements transform like products of the respective coordinates, they must remain unchanged under all the transformations listed. The mirror plane $m1$ changes x into $-x$ or y into $-y$, thus all elements with an odd number of indices 1 or an odd number of indices 2 have to be zero. The mirror plane $m2$ transforms x to y and y to x, thus elements where 1s are replaced by 2s have to be equal.

For the second order susceptibility tensor for second harmonic generation, e. g., we arrive at the nonzero elements

$$\chi_{311} = \chi_{322}, \quad \chi_{333}, \quad \chi_{131} = \chi_{113} = \chi_{232} = \chi_{223} \tag{3.14}$$

All other elements must be zero. Kleinman symmetry further reduces the number of independent elements to two (χ_{311} and equivalent, and χ_{333}).

3.1.8 Contraction of Indices

Especially for the susceptibility tensor for second harmonic generation it is common to write it in a different form. As the last two indices can be exchanged, there are 18 different elements left from the full set of 27. These 18 are written as a 2-dimensional matrix d_{ij} [27, 28, 30] , the last two indices kl of the elements χ_{ikl} are contracted to one index j such that

$$11 \to 1, \quad 22 \to 2, \quad 33 \to 3, \quad 23, 32 \to 4, \quad 13, 31 \to 5, \quad 12, 21 \to 6 \tag{3.15}$$

Using this matrix form of the susceptibility tensor, the second harmonic polarization is written as

$$\begin{pmatrix} P_x^{(2)}(2\omega) \\ P_y^{(2)}(2\omega) \\ P_z^{(2)}(2\omega) \end{pmatrix} = \varepsilon_0 \begin{pmatrix} d_{11} & d_{12} & d_{13} & d_{14} & d_{15} & d_{16} \\ d_{21} & d_{22} & d_{23} & d_{24} & d_{25} & d_{26} \\ d_{31} & d_{32} & d_{33} & d_{34} & d_{35} & d_{36} \end{pmatrix} . \begin{pmatrix} E_x^2(\omega) \\ E_y^2(\omega) \\ E_z^2(\omega) \\ 2E_y(\omega)E_x(\omega) \\ 2E_x(\omega)E_z(\omega) \\ 2E_x(\omega)E_y(\omega) \end{pmatrix} \tag{3.16}$$

Then the symmetry considerations in the case of SBN will lead to the following relations between the d tensor elements.

$$d_{31} = d_{32} = d_{15} = d_{24}, \quad d_{33} \tag{3.17}$$

Finally the SBN's d tensor is of the form:

$$d_{ij} = \begin{pmatrix} 0 & 0 & 0 & 0 & d_{15} & 0 \\ 0 & 0 & 0 & d_{24} & 0 & 0 \\ d_{31} & d_{32} & d_{33} & 0 & 0 & 0 \end{pmatrix} \tag{3.18}$$

3.2 Harmonic Generation

One of the most important nonlinear optical processes for technical applications is the generation of harmonics from laser light. We will discuss here second-harmonic generation, widely used for producing visible and near ultraviolet coherent light.

3.2.1 Second-Harmonic Generation

Second-harmonic generation (SHG) was the first experiment in the history of nonlinear optics carried out by Franken et al. [31] soon after the invention of the Ruby laser [32]. Presently it is one of the main applications of nonlinear optics, maybe the only really important one. In the preceding chapter some important points concerning the nonlinear susceptibility were presented. The general symmetry arguments have to be adopted in a suitable way for SHG. The responsible tensor is of third rank, materials for SHG thus must be non-centrosymmetric. For practical reasons, usually the d-tensor described is used instead of the more general χ-tensor.

The local second harmonic polarization can be calculated according to Eq. 3.9. For the generated second-harmonic intensity, yet, we face the phase-matching problem shortly discussed. Fig. 3.1 visualizes the principle.

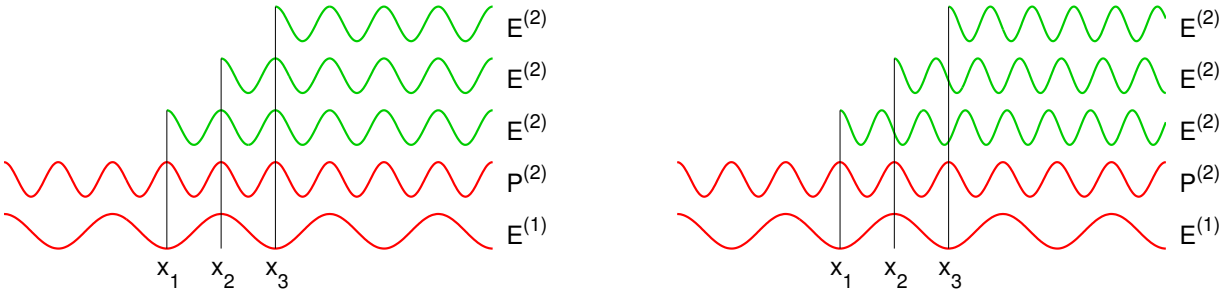

Figure 3.1: Fundamental wave $\mathbf{E}^{(1)}$, induced second-harmonic polarization $\mathbf{P}^{(2)}$, and second harmonic waves $\mathbf{E}^{(2)}$, generated at the positions x1, x2, and x3 in a nonlinear material for two different cases. Left: second-harmonic waves travel at the same velocity as the fundamental wave, all are in-phase throughout. Right: different velocities, the usual case, mismatch between the phases of the second-harmonic waves $\mathbf{E}^{(2)}$.

Due to dispersion present in all materials, waves of different frequencies travel at different velocities, yielding a phase-mismatch between second-harmonic waves generated at different positions in a nonlinear material. To get the total second-harmonic intensity produced, we have to integrate over the generated waves taking into account the different velocities. For simplicity were omit all rapidly oscillating factors and calculate only the phase-factors with respect to x = 0. For $E^{(1)}(x)$ and $P^{(2)}(x)$ can be written

$$\begin{aligned} E^{(1)}(x) &= E^{(1)}(0) \cdot e^{-ik_1 x}, \\ P^{(2)}(x) &= \chi \cdot E^{(1)}(x) \cdot E^{(1)}(x) = \chi \cdot E^{(1)}(0) \cdot E^{(1)}(0) \cdot e^{-i2k_1 x} \end{aligned} \tag{3.19}$$

Taking $P^{(2)}$ as driving force in a wave equation for $E^{(2)}$ yields

$$E^{(2)}(x) = K \cdot P^{(2)}(x) = K \cdot E^{(1)}(0) \cdot E^{(1)}(0) \cdot e^{-i2k_1 x} \tag{3.20}$$

where the K it contains all necessary constants like nonlinear susceptibility or refractive indices.

$E^{(2)}$ now travels through the material with a velocity characteristic for the frequency $\omega_2 = 2\omega_1$ and wave vector k_2. Thus at an arbitrary position x' where we could measure the second-harmonic

$$E^{(2)}(x') = E(2)(x) \cdot e^{-ik_2(x'-x)} = K \cdot E^{(1)}(0) \cdot E^{(1)}(0) \cdot e^{-ik_2 x'} \cdot e^{-i(2k_1-k_2)x} \tag{3.21}$$

Assuming a homogeneous material for $0 < x < L$, $E^{(2)}_{total}$ can be found integrating Eq. 3.21 over the length of the interaction between the fundamental light and the material

$$\begin{aligned} E^{(2)}_{total}(x') &= K \cdot E^{(1)}(0) \cdot E^{(1)}(0) \cdot e^{-ik_2 x'} \int_0^L e^{-i(2k_1-k_2)x} dx \\ &= K \cdot E^{(1)}(0) \cdot E^{(1)}(0) \cdot e^{-ik_2 x'} \tfrac{1}{i\Delta k} \left[e^{i\Delta k L} - 1 \right] \\ &= K \cdot E^{(1)}(0) \cdot E^{(1)}(0) \cdot e^{-ik_2 x'} \cdot e^{i\frac{\Delta k}{2}L} \tfrac{1}{i\Delta k} \left[e^{i\frac{\Delta k}{2}L} - e^{-i\frac{\Delta k}{2}L} \right] \\ &= K \cdot E^{(1)}(0) \cdot E^{(1)}(0) \cdot e^{-ik_2 x'} \cdot e^{i\frac{\Delta k}{2}L} \cdot \tfrac{\sin(\Delta k L/2)}{\Delta k/2} \end{aligned} \tag{3.22}$$

with

$$\Delta k = k_2 - 2k_1 = \frac{2\pi}{\lambda_2} n(\omega_2) - 2\frac{2\pi}{\lambda_1} n(\omega_1) = \frac{4\pi}{\lambda_1}(n(\omega_2) - n(\omega_1)) \tag{3.23}$$

λ_1 and $\lambda_2 = \lambda_1/2$ are the wavelengths of the fundamental and second harmonic waves, respectively, in vacuum.

Often a characteristic length, the so-called *coherence length* L_c, is defined. Yet one has to be careful as two different definitions are used - the length after which the sine reaches its maximum or the length after which the sine changes sign. Thus it may be defined as

$$\text{either} \quad L_c = \frac{\pi}{\Delta k} \quad \text{or} \quad L_c = \frac{2\pi}{\Delta k} \tag{3.24}$$

The generated second-harmonic intensity depends mainly on the phase mismatch Δk, and of course on the square of the input intensity and the tensor elements involved. For the

latter often a so-called effective tensor element is used which is a suitable combination for the geometry considered

$$I^{(2)} = C \cdot d_{eff}^2 \cdot I^{(1)^2} \cdot \frac{\sin^2(\Delta k L/2)}{(\Delta k/2)^2} \tag{3.25}$$

For numerical calculation of $I^{(2)}$ an appropriate constant C may be adopted from textbooks on nonlinear optics.

In generall Δk in Eq. 3.25 is non-zero, the intensity oscillates in a sine-square way. If, however, Δk approaches zero, we have to calculate the limit

$$\lim_{\Delta k \to 0} \frac{\sin(\Delta k L/2)}{\Delta k/2} = L \tag{3.26}$$

In this case, the second-harmonic intensity increases quadratically with L - at least as long as we are in the limit of low second-harmonic intensities where $I^{(1)}$ is unchanged (undepleted fundamental wave approximation). The spatial variation of second-harmonic intensities for some characteristic values Δk is sketched in Fig. 3.2

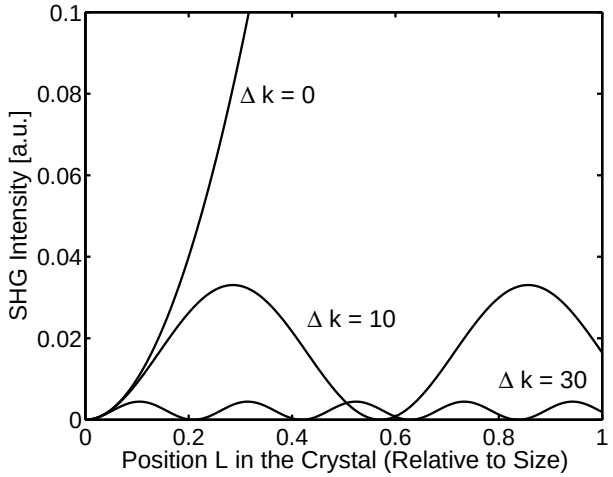

Figure 3.2: Second-harmonic intensities as a function of the position in the nonlinear material for different Δk.

3.2.2 Phase Matching

For an efficient generation of second-harmonic light it is highly desirable to achieve phase matching, $\Delta k = 0$. Usually the refractive indices are governed by normal dispersion which means that in Eq. 3.23 the difference $n(\omega_2) - n(\omega_1)$ is larger than zero, revealing $\Delta k > 0$. One way out is to utilize the birefringence which is present in crystals of all symmetry

classes except the cubic one. Uniaxial classes with two different principal refractive indices include the tetragonal, hexagonal and trigonal ones; biaxial classes, where all three principal indices are different, include the orthorhombic, monoclinic and triclinic ones.

The refractive index of a material is derived from the linear susceptibility, a second rank tensor. This tensor can be visualized by a general ellipsoid - general means that all three axes of the ellipsoid are of different lengths and that the orientation is arbitrary. However, this ellipsoid has to be compatible with the point symmetry of the material regarded. That means that certain symmetry elements may fix the orientation of the ellipsoid and may force two or all three axes to be equal. This reveals the above classification. In all uniaxial classes, the orientation of the ellipsoid is fixed, and the ellipsoid is rotationally symmetric. In the biaxial classes where all three axes are different in length, the orientation is fixed for orthorhombic crystals, one axis is fixed for monoclinic crystals, and the orientation is completely free for triclinic ones. For the latter two cases, moreover, the orientation is wavelength dependent.

The **k**-vector of light propagating in the material defines a plane perpendicular to it through the center of the ellipsoid. This plane intersects the ellipsoid yielding an ellipse as intersection curve. The directions of the major and minor axes of this ellipse define the two polarization directions allowed, the length of these axes determine the respective refractive indices. These two different indices for every crystallographic direction can be plotted as index surfaces which reveal the two refractive indices as intersections with the respective **k**-vector direction.

This directional dependence of the refractive indices for the uniaxial case is shown in Fig. 3.3 (left). For every direction of the wave vector in an uniaxial crystal two different refractive indices are found which are valid for the two light polarizations possible.
The two refractive indices define the two possible velocities of light - a maximal and a minimal one - for every propagation direction. Two fixed polarization directions inside the crystal, perpendicular to each other, are connected with the two refractive indices. There are obvious distinct exceptions to this general rule of two different refractive indices. In Fig. 3.3 (left) one can see that for light propagating along the crystallographic z-axis only one refractive index is found. For these special propagation directions arbitrary light polarizations are possible. These crystallographic directions are called the optic axes.

Utilizing the birefringence of a material, it may be possible to find propagation directions where the velocities of fundamental and harmonic waves are identical. Drawing the index surfaces for fundamental and harmonic frequencies, these directions are found as the intersection curves between the index surfaces.

Fig. 3.3 (right) shows this for an uniaxial material. The index surfaces for the ordinary index at the fundamental frequency, $n_o^{(1)}$, and for the extraordinary index at the harmonic frequency, $n_e^{(2)}$, are sketched, the intersection curve is a circle, all propagation directions

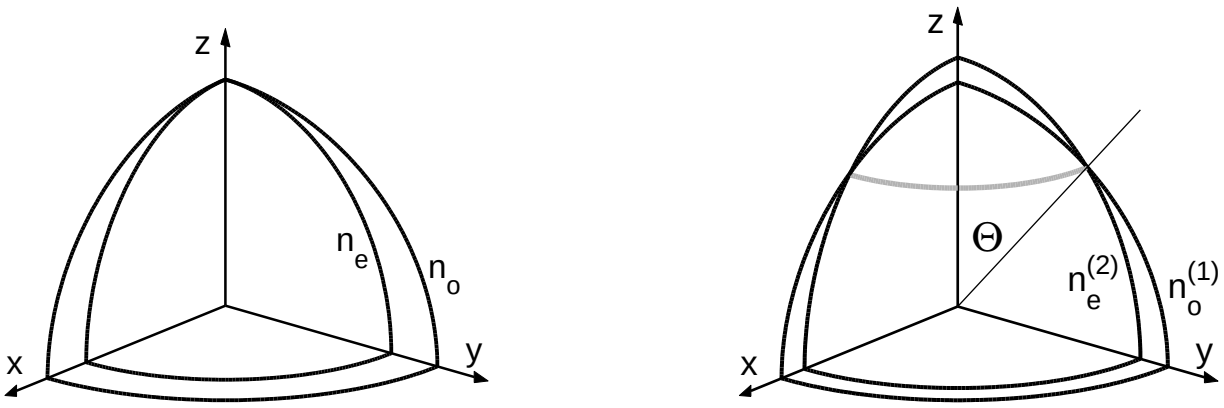

Figure 3.3: *Left:* Refractive index surfaces in an uniaxial crystal. The two surfaces indicate the refractive indices for the respective crystallographic directions.
Right: Refractive index surfaces for the ordinary index at the fundamental frequency, $n_o^{(1)}$, and for the extraordinary index at the harmonic frequency, $n_e^{(2)}$ in a uniaxial material with so-called negative birefringence ($n_e < n_o$). The gray intersection curve (circular in the uniaxial case) determines the phase-match angle Θ.

with a fixed angle Θ versus the z-axis are phase-matched.

To check whether phase matching is really possible, one has to consider the dispersion behavior of the material. Typical dispersion curves for uniaxial crystals are sketched in Fig. 3.4. A fundamental wavelength of 1000 nm, consequently a harmonic at 500 nm are assumed. Low birefringence (left) inhibits phase matching, higher birefringence (right) allows it. Or, every birefringent material has a certain restricted wavelength range with a characteristic short-wavelength limit, in which phase-matching is possible.

The refractive index of the harmonic beam is defined as a function of the angle Θ as

$$\frac{1}{n^2(\Theta)} = \frac{\cos^2(\Theta)}{n_0^2} + \frac{\sin^2(\Theta)}{n_e^2} \tag{3.27}$$

From Eq. 3.27, in turn the phase-matching angle Θ can be deduced demanding a value $n(\Theta)$ at the harmonic wavelength to be equal to n_o at the fundamental wavelength. A real solution for Θ then indicates that we are inside the wavelength range where phase matching is possible.

The above considerations assume that the two relevant fundamental waves are identical. This is referred to as *Type I* phase matching. Instead, two different fundamentals can be combined which usually are split from one incident wave. We then speak of *Type II* phase matching.

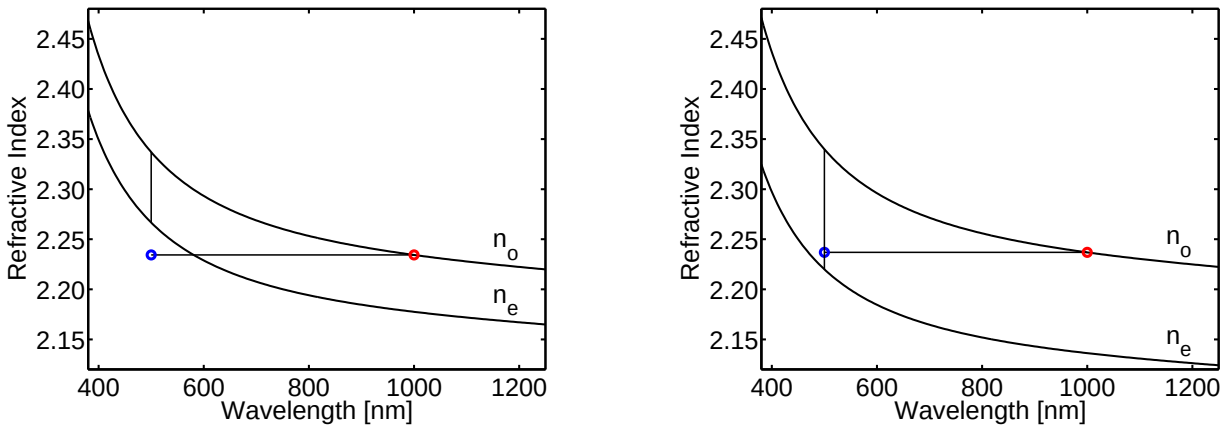

Figure 3.4: Dispersion of the refractive indices in uniaxial crystals. Left: low birefringence, right: higher birefringence. The refractive index for the ordinary fundamental wave is fixed, the index for the extraordinary harmonic wave can be angle-tuned along the vertical lines drawn.

3.2.3 Quasi Phase Matching

Already in one of the first theoretical publications on nonlinear optics [33], Bloembergen and coworkers discussed a different method to achieve phase matching for nonlinear optical processes, especially for second-harmonic generation. They proposed to reverse the sign of the respective tensor element periodically after an appropriate crystal thickness. In ferroelectric materials this can be done by an antiparallel poling of crystal regions, ferroelectric domains. The geometry for a typical example is sketched in Fig. 3.5

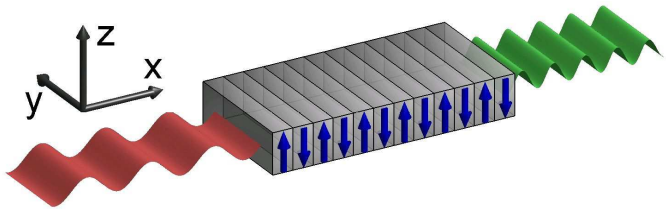

Figure 3.5: Periodically poled domain structure for second-harmonic generation in materials like lithium niobate or lithium tantalate.

The usage of such periodically poled structures is commonly referred to as *quasi phase matching*. The momentum conservation law is fulfilled with the help of the additional vector $\mathbf{K}$ which describes the periodicity of the antiparallel domains:

$$\mathbf{k}_2 = \mathbf{k}_1 + \mathbf{k}_1' + \mathbf{K} \tag{3.28}$$

The second-harmonic intensity achieved through the periodically poled geometry is de-

picted in Fig. 3.6. The intensity dependencies are calculated for phase-matched, quasi-phase-matched, and non-phase-matched conditions under the assumption of identical tensor elements d involved.

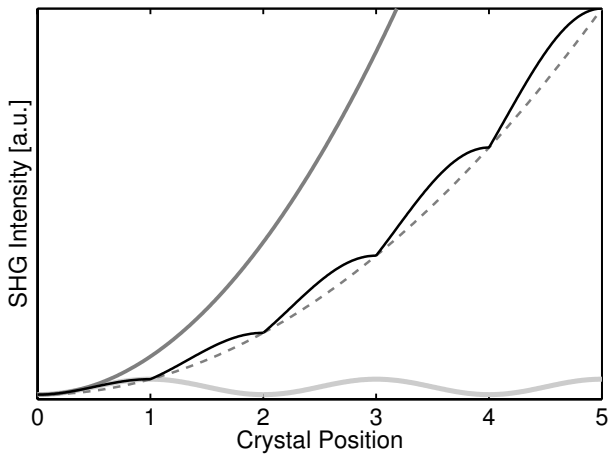

Figure 3.6: Intensities of phase-matched (dark gray parabola), quasi-phase-matched (black curve), and non-phase-matched SHG (light gray), assuming identical tensor elements and identical beam geometries.

They gained increasing interest in the recent years because of several reasons:

- Successful techniques for the fabrication of periodically poled structures have been developed [34]
- Nonlinear optical materials - especially lithium niobate and lithium tantalate - have been improved to facilitate poling.
- The demand for doubling of low light intensities has increased due to the rapid development of semiconductor lasers.
- Quasi phase matching extends the wavelength range for nonlinear optical processes up to the full transparency range of the material.

It should be emphasized that the technique is only applicable to ferroelectric nonlinear optical materials, thus is not suitable for a number of classical materials. And periodically poled structure is also usable for higher order harmonics [35].

3.3 Known SHG Schemes

The principles of harmonic generation introduced up to this point refer in particular to the case of Second Harmonic Generation (SHG). In the following chapters the practical schemes of SHG and some applications where these can be used will be presented.
Usually nonlinear optical processes are regarded to be collinear which means that all participating light beams are pointing approximately into the same direction. Such collinear geometries have the advantage of large interaction lengths, thus optimize the efficiency of the nonlinear interaction.
However, it's not a must to work with collinear beams, non-collinear interactions are possible as well. As the interacting beams are inclined to each other, the intersection volume will be small, the resulting short interaction length will hamper efficiency. Non-collinear geometries are therefore not suitable for efficient frequency conversion, they are only interesting for their physics and they can be useful for material characterization.

3.3.1 Collinear Second Harmonic Generation

Perhaps the most useful scheme and also the most simple to describe is called **Collinear Second Harmonic Generation**. For such a case a nonlinear medium is needed. And a crystal with as large value as possible of the d tensor elements. Beside this the crystal must be anisotropic, the birefringence $\Delta n = n_e - n_o$ has to be large enough to fulfill the phase matching condition. That means that the refractive index for the generating wave n_{IR} must be equal to the refractive index of the generated second harmonic light n_{SHG}.
If one considers the case of an incident beam with a wavelength $\lambda_{IR,0} = 1064$ nm of an infrared Nd:YAG laser then second harmonic light with $\lambda_{SHG,0} = 532$ nm will be generated. This is the usual way for getting green lasers out of the widely used Nd:YAG ones.

The refractive index condition is just a different aspect of the momentum conservation for the SHG generation process. One can observe that the energy conservation leads to the double frequency of the generated light compared to the incoming one. The two laws can be expressed as following

$$\sum_i \omega_i = 0, \quad \sum_i \mathbf{k}_i = 0 \tag{3.29}$$

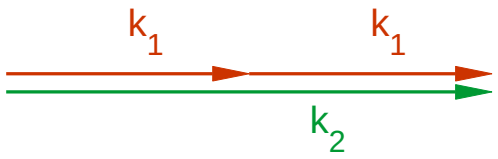

Figure 3.7: Momentum conservation for the collinear Second Harmonic Generation.

One can observe that in this scheme of harmonic generation the momentum is conserved not just as a vector but as a scalar as well. Or in other words the sum of the lengths of the two infrared light momentum vectors is equal to the length of the generated light momentum vector (Fig. 3.7). This is a consequence of the fact that in this case $n_{IR,o}$ and $n_{SHG,e}$ are equal. Due to the long interaction length between the fundamental light and the nonlinear medium this scheme is used for frequency conversion [27, 28, 36]. Typical crystals for this application are KDP, KTP, PPLN.

3.3.2 Non-Collinear Second Harmonic Generation

3.3.2.1 Induced Non-Collinear SHG

The first non-collinear SHG process described is called **Induced Second Harmonic Generation**. This technique utilizes two fundamental light beams inclined to each other to fulfill the vectorial phase matching condition, the momentum conservation sketch is like in the Fig. 3.8

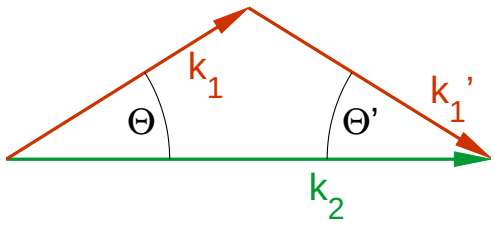

Figure 3.8: Vectorial momentum conservation for Induced Second Harmonic Generation.

$$\mathbf{k}_2 = \mathbf{k}_1 + \mathbf{k}_1' \tag{3.30}$$

The length of the generated vector k_2 is less than the sum of the lengths of k_1 and k_1'. That is only possible for crystals of larger birefringence than the one needed for the collinear case. Of course the collinear case can also be fulfilled in such a crystal by choosing a certain angle so that the birefringence is decreased and suited for the collinear scheme.

The vectorial phase matching condition Eq. 3.30 can be referred to a condition for the respective refractive indices n_{SHG} and n_{IR}. The two fundamental beams usually are derived from the same laser which means that the light waves with the k vectors $\vec{k_1}$ and $\vec{k_1'}$ have the same frequencies. Furthermore, a geometry can be chosen where the two fundamental beams are arranged symmetrically with respect to the index ellipsoid and have symmetric polarization, then the momentum conservation Eq. 3.30 will lead to a relation of the refractive indices like:

$$n_{SHG}(\mathbf{k}_2) = n_{IR}(\mathbf{k}_1)\cos(\Theta) \tag{3.31}$$

The angle Θ and the polarizations of the incident beams have to be chosen in an appropriate way to fulfill Eq. 3.31. Obviously this condition is very sensitive to variations in the refractive indices.

As it was mentioned at the beginning of this chapter two fundamental light beams inclined to each other are the input beams and the interaction volume is limited in all three spatial dimensions. Thus such an experiment can be used to get information just about the volume element under illumination. Moving the sample in all spatial directions yields a fully three-dimensional topography. The resolution depends on the beam geometries and on the angle Θ.

The technique may be illustrated by two typical applications concerning the characterization of optical crystals: composition measurements in lithium niobate [37,38] and detection of domain borders in potassium niobate [39].

3.3.2.2 Spontaneous Non-Collinear SHG

In contrast to induced non-collinear frequency doubling, spontaneous non-collinear frequency doubling is a type of optical second harmonic generation that uses randomly scattered light to provide additional fundamental beams in order to accomplish non-collinear phase matching [40]. This scattered light may arise from the crystal itself due to inhomogeneities or impurities or may be forced by suitable optics (ground glass plate in front of the sample). The corresponding momentum diagram is shown in Fig. 3.9 Again the vectorial phase matching condition described by Eq. 3.30 has to be fulfilled.

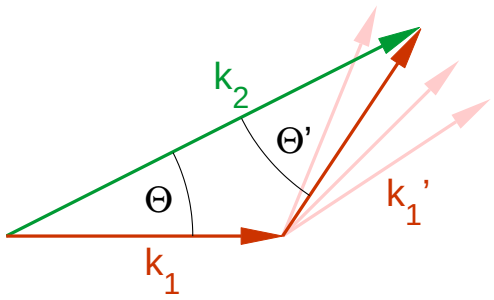

Figure 3.9: Vectorial momentum conservation for Spontaneous Second Harmonic Generation.

As light is scattered in all three-dimensional directions, phase matching now can be achieved for a multitude of angles $\Theta + \Theta'$ around the direction of the fundamental beam. This leads to a cone of second harmonic light. The cone angle Θ depends on the crystallographic direction and the respective effective refractive indices. To keep it simple, the fundamental beam is directed along one of the axes of the index ellipsoid yielding a cone of approximately elliptic shape. The ellipsoid parameters depend very sensitively on the refractive

indices for the fundamental and the second harmonic light at the position of the focused fundamental light beam. Thus a two-dimensional topographical characterization of crystals is possible when the sample is moved perpendicular to the fundamental beam direction. The spatial resolution depends on the fundamental beam geometry.

Again, two examples may illustrate the application of the technique for material characterization, the homogeneity and composition measurement of a pure lithium niobate crystal and the characterization of so-called growth striations in Mg-doped lithium niobate. Of course this SHG scheme is suited just for the crystals with a large birefringence [40].

3.3.2.3 Conical Harmonic Generation

An interesting mechanism for the generation of harmonic light is the use of higher order nonlinearities. This mechanism for Conical Harmonic Generation was described and experimentally verified in 2002 by Moll et al [41]. The wave vector geometry for second-harmonic generation via this mechanism is shown in Fig. 3.10

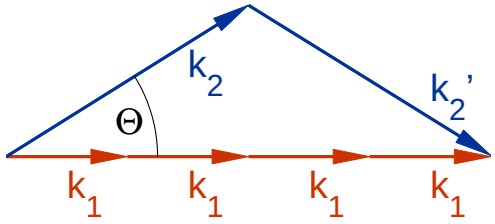

Figure 3.10: Vectorial momentum conservation for the Conical Harmonic Generation.

Five waves $(4 \times k_1, k_2')$ have to interact to produce a second harmonic wave k_2. As k_2' also has to be generated by the fundamental pump wave k_1, the whole process can be regarded as parametric amplification of a signal and an idler beam, k_2 and k_2' respectively. As usual for parametric amplification, the theoretical description consists of three coupled equations for the three interacting waves k_1, k_2, k_2'. Generally, the two generated waves may be of different frequencies, most effective amplification is achieved, however, when the frequencies of signal and idler are identical. A comprehensive treatment is given in the above cited publication.

The wave vector geometry in Fig. 3.10 shows that for the generation of the second order harmonic a 5^{th} order nonlinear interaction is responsible. This can be generalized: radiation at the m-th order harmonic can be generated through the use of a $(2m+1)$- order nonlinearity. The tensor of the corresponding nonlinear susceptibility is of rank $(2m+2)$, always of even rank. Thus this process allows for the generation and amplification of both odd- and even-order harmonics in all materials, even in isotropic ones. Additionally, this process can always be phase matched in normal-dispersion materials without the use of birefringence. From the wave vector diagram it can be derived:

$$\cos\Theta = n(\omega)/n(2\omega) \tag{3.32}$$

or for the generation of the m-th order harmonic:

$$\cos\Theta = n(\omega)/n(m\omega) \tag{3.33}$$

Both equations can always be fulfilled for normal dispersion as in this case $n(m\omega) > n(\omega)$. This is the only SHG scheme that can be fulfilled in any material, no high birefringence is required not even anisotropy of the crystal. It must be underlined that the second harmonic light generated with this method is always a **cone** with a certain angle Θ.

In the previous chapters the importance of the refractive index or of the birefringence in the SHG process was pointed out. This parameter is the one determining which scheme of harmonic generation can be realized in the considered nonlinear medium.
As a summary one can review that the Collinear, Induced and Spontaneous schemes are compatible just with the case of large birefringence and only the Conical harmonic generation can be obtained in any case.
For the determination of the second harmonic generation scheme present in the case of SBN first refractive index measurement have to be performed. Therefore the following section will be dedicated to these measurements.

Chapter 4

Refractive Index for SBN

4.1 Introduction

One of the first measurements of the refractive index of $Sr_xBa_{1-x}Nb_2O_6$ was made in 1968 by Venturini et al [42]. Crystals with compositions $x = 0.25$, $x = 0.50$ and $x = 0.75$ have been used. Values of other compositions as well as the congruently melting one could be obtained just by an interpolation of these data. Later, other measurements have been performed on several compositions in single domain crystals [43, 44]. None of these measurements covers the whole composition range where the crystal can be grown and in all cases just very few wavelengths were available.

4.2 Measurements and Results

In this work refractive index measurements for as-grown SBN crystals covering not only the entire composition range but also a wide wavelength region from infrared to near ultraviolet are presented.
Eleven triangular prisms have been prepared with the composition varying from $x = 0.32$ to $x = 0.79$ (*in the work of Venturini et al [42] the values of x are given as they were in melt but in our case the values are those in the crystal, obtained with measurements of X-Ray fluorescence [21].*). The c-axis is oriented perpendicular to the two parallel surfaces using a {100} growth face as a reference. All sides were polished to optical quality.

Using the minimum deviation method the refractive indices were determined with an absolute accuracy better than ± 0.002 for the case of the visible and the near ultraviolet. The accuracy for the relative far infrared is somewhat worse due to the detection of the image. For the visible a mercury-lamp and for the infrared measurements two laser diodes of 790 nm and 1500 nm were used. In the case of the second laser diode a suitable infrared camera has been adapted to the goniometer. All measurements were carried out at room temperature (T = 22 °C) and the light intensity was kept low to avoid heating of the

Compositions [x]	0.34	0.41	0.48	0.51	0.56	0.61	0.64	0.69	0.74	0.77	0.79

Table 4.1: Compositions used for refractive index measurements of $Sr_xBa_{1-x}Nb_2O_6$

Wavelength [nm]	435.8	467.8	480.0	508.6	546.1	578.0	643.8	790.0	1500.0

Table 4.2: Wavelengths used for refractive index measurements. The first seven wavelengths were obtained from a mercury-lamp, last two 790 nm and 1500 nm are from infrared laser diodes.

Type	A	B $[nm^2]$	C $[nm^2]$	D $[nm]$
Extraordinary	$4.74 + 0.38 \cdot x$	$1.02E5 + 1.48E4 \cdot x$	$4.72E4 + 2.67E4 \cdot x$	$-2.14E\text{-}5 \cdot x$
Ordinary	5.11	1.18E5	6.69E4	0

Table 4.3: Coefficients of the Sellmeier equation Eq. 4.1 used for the global fit of the refractive indices. For the extraordinary fit the coefficients are depending on the Strontium - Barium ratio in the crystal. Thus they are expressed as functions of the Strontium fraction x. The ordinary indices are independent of this ratio.

samples.
Table 4.1 presents the list of the composition for the samples used and in table 4.2 the wavelengths are summarized where the measurements were carried out.
Figure Fig. 4.1 shows the dispersion, the fitting curves, of extraordinary (n_e) and ordinary (n_o) refractive indices. The upper-most solid curve represents the ordinary refractive indices n_o for all compositions. The lower curves are for the extraordinary indices n_e. The curve just below the solid, ordinary one, is for the sample with the composition $x = 0.79$. The values of the extraordinary indices are decreasing monotonically. Thus the lowest curve represents the extraordinary dispersion for the composition $x = 0.32$.

A global fit was made over the whole composition range using a conventional four-parameter Sellmeier equation Eq. 4.1. A good fit can be made assuming that all coefficients of this equation are linear functions of the composition x.

$$n^2(\lambda) = A + \frac{B}{\lambda^2 - C} + D\lambda \tag{4.1}$$

Table 4.3 presents the four coefficients of the Sellmeier equation used to fit the data.
Figure Fig. 4.2 shows a global fit for the extraordinary index n_e over the whole composition range and over all measured wavelengths.

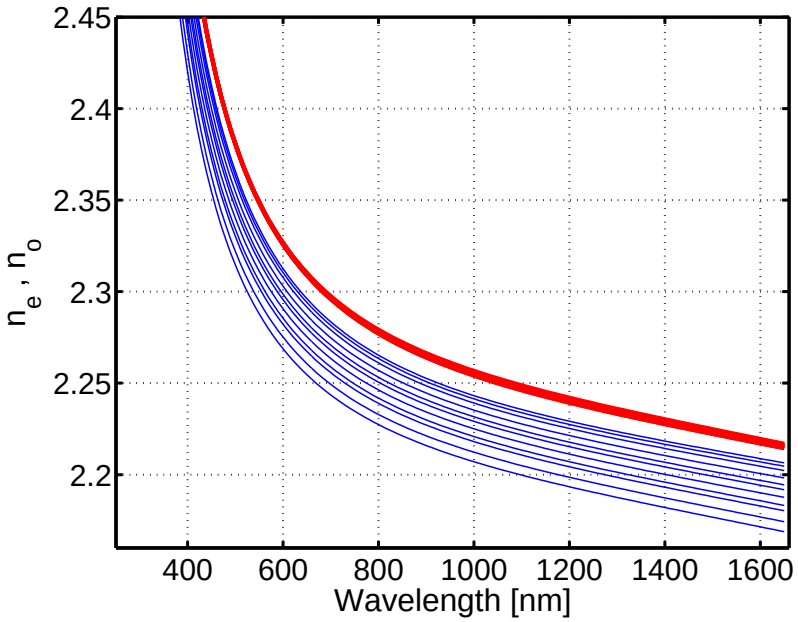

Figure 4.1: Ordinary and extraordinary refractive indices for $Sr_xBa_{1-x}Nb_2O_6$. The uppermost solid curve represents the ordinary dispersion for all the compositions $0.32 < x < 0.79$. The rest of the curves are the extraordinary dispersions for the eleven crystals measured. The lowest one corresponds to $x = 0.32$ and the one just below the ordinary curve is for the most Strontium rich sample $x = 0.79$.

Only a very slight dependence can be found for the ordinary refractive index as a function of composition x. Figure Fig. 4.3 presents a magnified picture of the n_o curves around the wavelength 690 nm. The highest values are those for the sample with $x = 0.79$ and the lowest curve represents the ordinary refractive indices for $x = 0.32$. One can observe that the differences between values of the refractive index are in the measurement error range, thus it makes no sense to fit the parameters of the Sellmeier equation with composition as was done in the case of the extraordinary indices.
The birefringence is presented in Fig. 4.4. Considering the ordinary refractive indices independent of composition, then like the extraordinary indices also the birefringence is a monotonic function of x. The largest birefringence is for the crystal containing the highest concentration of Barium.
However, also in this case the birefringence is one of the smallest of all known tetragonal Tungsten-Bronze structures [45, 46]

It is known from the literature that in case of SBN there is no relevant difference of the refractive indices between the poled and unpoled material. Therefore and also due to the difficulties which can arise for a high temperature poling of the Barium rich compositions it was preferred to perform all the measurements in the as-grown state.

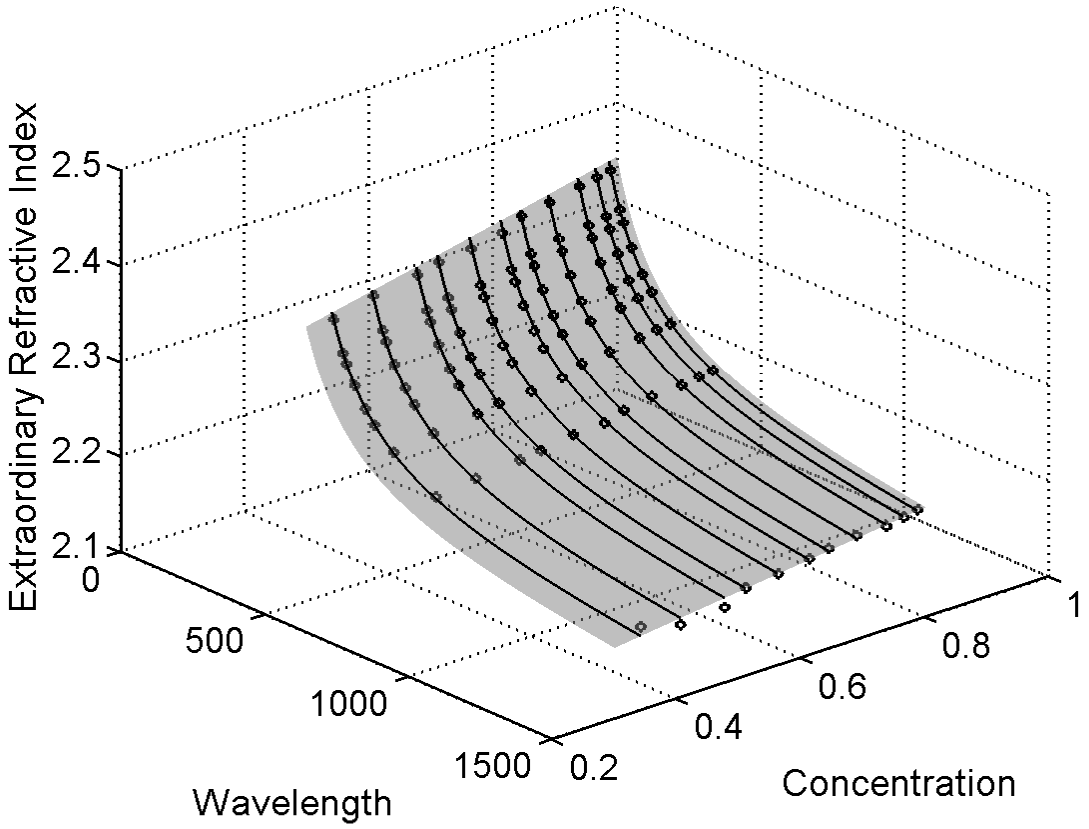

Figure 4.2: Global fit of the extraordinary refractive indices over the whole composition range where the crystal can be grown and over all measured wavelengths. The circles are the measured values and the eleven lines represent the values of the global fit at the measured compositions.

4.3 Phase Matching calculation

Using Eq. 4.1 one can calculate for which composition of the SBN crystal and what wavelength region phase matching for second harmonic generation (SHG) is possible. The gray region in figure Fig. 4.5 shows the phase matching possibilities for a wavelength region of the fundamental beam between 1200 nm and 1650 nm. The required composition of the crystal is below $x = 0.26$. From the phase diagram of the crystal [21] one can see that this requirement can not be fulfilled. The tetragonal Tungsten-Bronze SBN crystal can only be grown in a composition range of $0.32 < x < 0.79$.

From the refractive index measurement it is evident that no known second harmonic scheme can be responsible for the harmonic generation in SBN. Due to low birefringence none

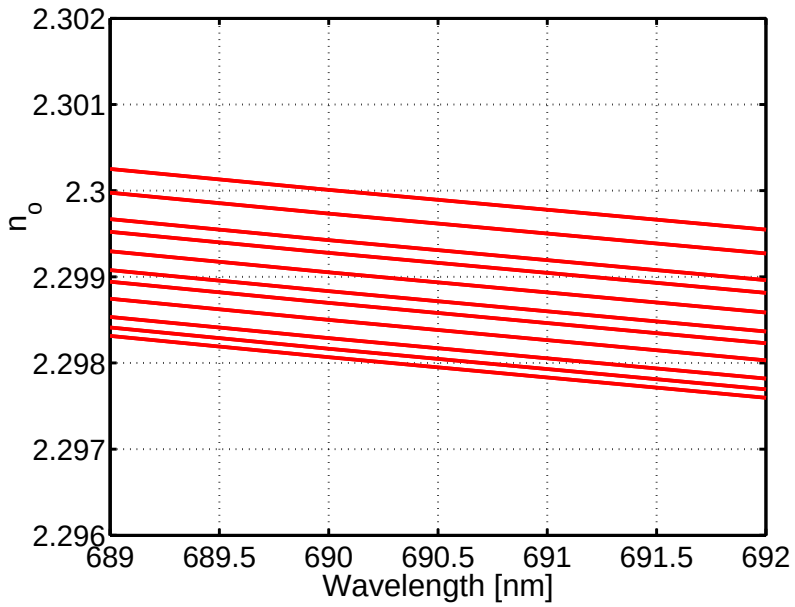

Figure 4.3: Ordinary refractive indices around a wavelength of $690nm$. The Strontium fracion x decreases from the upper to the lower curves. One can see that the composition dependence of the ordinary refractive index is in the measurement error range. Therefore no composition dependence is included in the fit for the ordinary index.

of the collinear, induced or spontaneous SHG schemes can play any role in case of this crystal. Only the Conical harmonic generation could always be accomplished independent of birefringence, but as shown in section 3.3.2 the result of this process would always be a harmonic cone of a certain angle, and this is not the case for SBN. The next chapter at first will present experimental observations about the generation of a second harmonic in the case of SBN. In the second part of the chapter a novel model will be proposed to explain the harmonic generation.

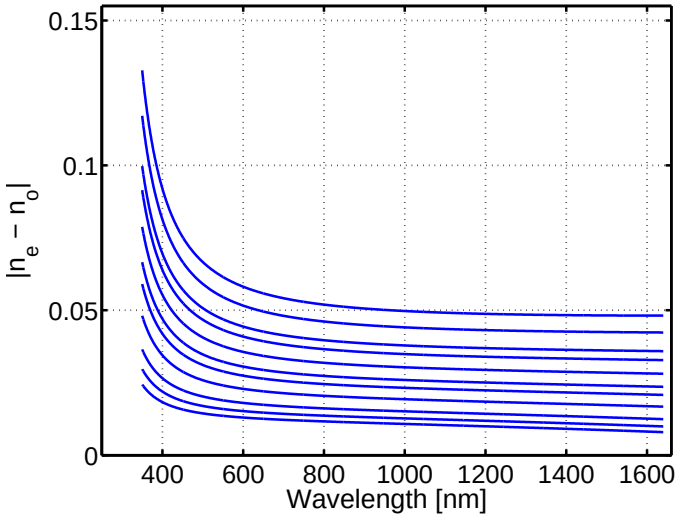

Figure 4.4: Absolute values of birefringence $|n_e - n_o|$ vs. light wavelength. The eleven lines represents the birefringence for the measured samples. The highest values are for the sample containing the most Barium. Birefringence monotonically decreases with increasing Strontium content in the sample. The plots have been made using the Sellmeier equation Eq. 4.1 and the parameters from table Tab. 4.3

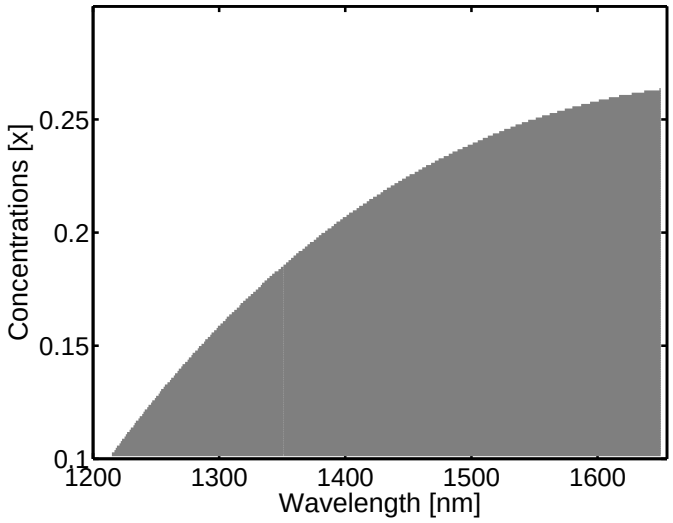

Figure 4.5: Second harmonic phase matching in SBN. The grayed area represents the compositions and wavelengths of the fundamental beam where phase matching is possible. The required composition for phase matching is below $x = 0.26$. From the phase diagram [21] one can see that is not possible to grow tetragonal Tungsten-Bronze SBN crystals with a value of x less than 0.32.

Chapter 5

Domain Induced Second Harmonic Generation (DISHG)

As shown in the previous chapter phase matching for collinear SHG is not possible in SBN. Nevertheless intense green light is observed when the crystals are illuminated with the beam of a pulsed Nd:YAG laser.

5.1 Experimental Observations

Most of the second harmonic experiments were carried out using a Nd:YAG pulse laser, with pulses of 5 ns, a repetition rate of about 1 KHz, wavelength of 1064 nm and approximately 10 KW peak power.

5.1.1 Planar noncollinear SHG

When the incident laser light is directed perpendicular to the c-axis of the SBN crystal one can experience green extraordinary polarized second harmonic light emitted in all directions in the (c) plane (Fig. 5.1).

The polarization state of second harmonic light can be easily deduced considering the d-tensor's nonzero elements. While entering the crystal with a beam perpendicular to its c-axis and parallel to its b-axis the electric field vector of the infrared laser light must be in the (ac) plane or in other words the components of the electric field vector are those with indices 1 and 3. From 3.16 it can be seen that for all polarizations of the infrared laser beam the excited nonlinear polarization in the crystal is along the c-axis. Thus the polarization state of the generated second harmonic light is extraordinary.

The measurements show that the second harmonic intensity for extraordinarily polarized incident light is larger than for ordinary one. That means that d_{33} is larger than the other

tensor elements.

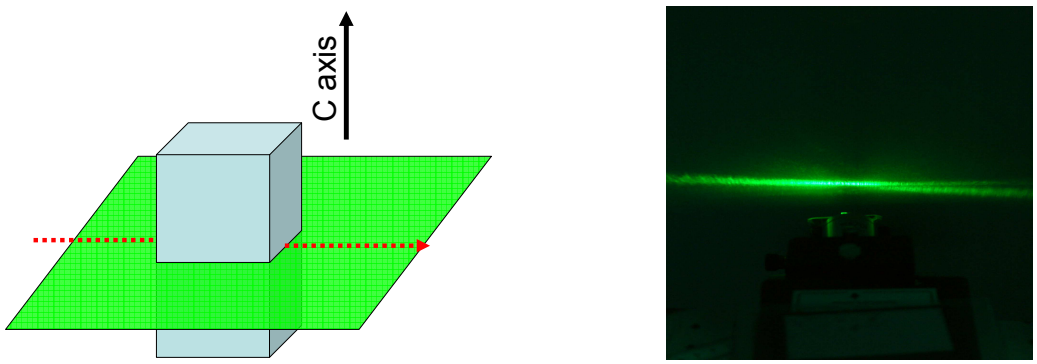

Figure 5.1: SHG in SBN, on the left side the case of the laser beam perpendicular to the crystallographic c-axis is sketched, in this case a continuous and homogeneous distribution of SHG can be observed perpendicular to the direction of the c-axis. On the right is a picture of this experiment. The bright line is the intersection between the second harmonic plane and the projection screen. (The infrared light can not be seen, it was supressed with an appropriate filter.)

Back to the observations and after explaining the SHG light polarization it is still the question of the light distribution which is nearly homogeneous in a plane perpendicular to the c-axis (Fig. 5.2 *center*). The first idea to explain this was that SHG is generated in a collinear way and then due to scattering on the domain walls this homogeneous distribution results. This model would also work for poled samples. In this case the SHG intensity is still distributed in the (c) plane but the intensity is no longer isotropic regarding the angular distribution, more can be seen at angles of 0° and 180° to the direction of the laser beam and less at (90° Fig. 5.2 *right*).
This could be explained by less scattering in the poled samples due to much less domain walls.

5.1.2 Conical non-collinear SHG

The 'scattering model' was satisfying up to a day when the crystal was turned with the c-axis parallel to the beam direction. In this case a green circle was seen on the projection screen (Fig. 5.3).

Placing an analyzer between the crystal and the projection screen shows that the ring is radially polarized. The circular symmetry of the polarization pattern can be confirmed by roating the analyzer (Fig. 5.4).

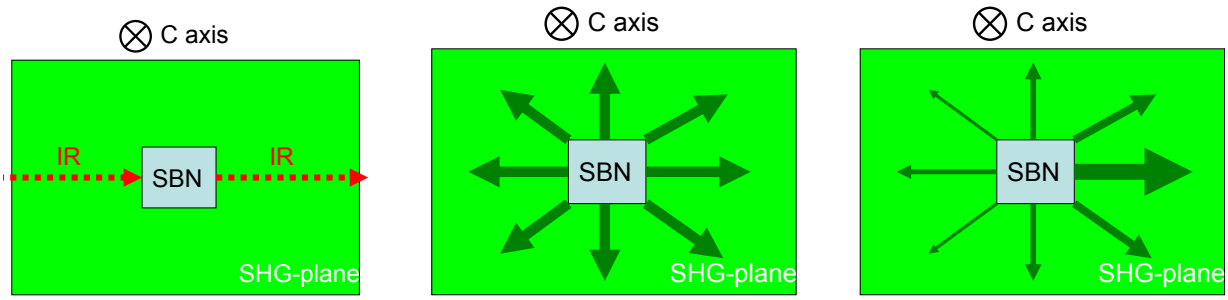

Figure 5.2: SHG in SBN with the laser light perpendicular to the c-axis and propagating along the b-axis of the crystal. All three pictures present a c-cut of an SBN crystal.The left image shows the propagation of the laser beam. The center image presents the second harmonic generation of an as-grown SBN crystal. Here the second harmonic is distributed homogenously in all directions. The picture from the right presents second harmonic generation of a poled SBN crystal. Here the main SHG intensity is in forward direction and less at different angles.

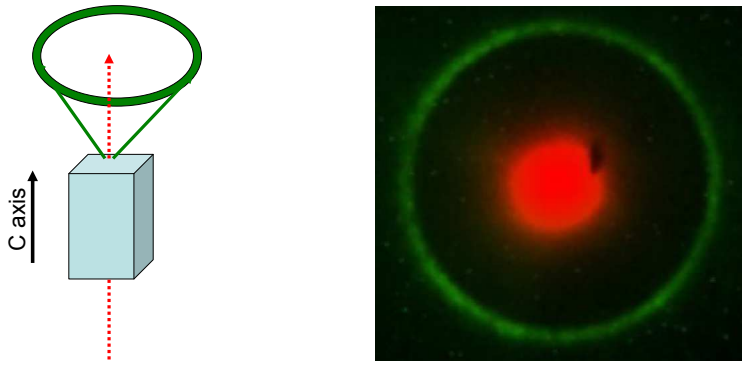

Figure 5.3: Case of SHG in SBN with the laser light travelling in the crystal along the ferroelectric c-axis. On the left the geometry is sketched. The dashed arrow represents the infrared light. The solid lines, sketching a cone, represent the generated second harmonic light. On the right image a photo of the screen picture is presented. The middle bright spot is the infrared and the bright circle is the intersection of the second harmonic cone with the screen.

Similar ring-shaped patterns are found in a vast variety of so-called parametric scattering processes in photorefractive crystals [47–49]. Although SBN is one of the most interesting photorefractive materials, parametric scattering in combination with harmonic generation can be excluded as an explanation due to two main reasons. First, the photorefractive response of a material arises from suitable impurities – we used undoped crystals. Second, the onset of parametric scattering processes always shows a temporal evolution. To check this point, we measured the time shape of the ring signal at the very first laser pulse and at

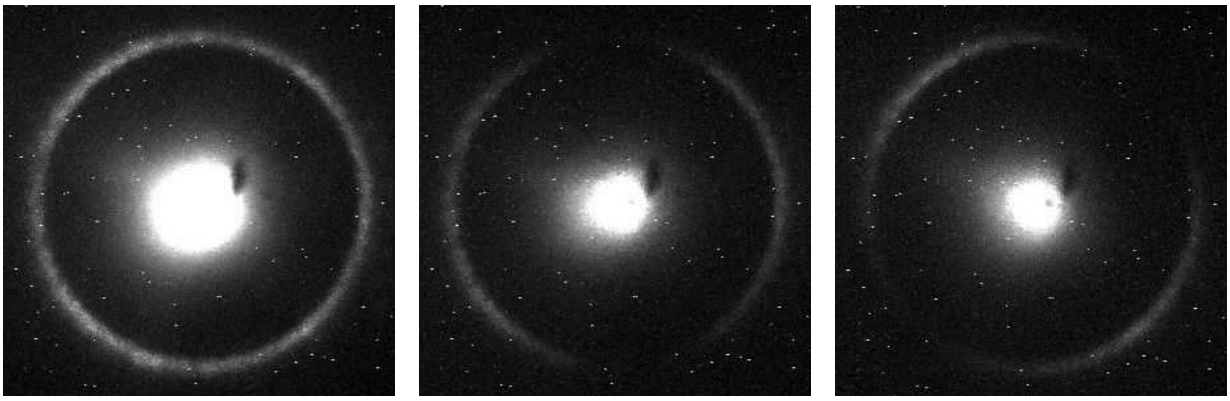

Figure 5.4: Polarization properties of the SHG ring. Left: without analyzer, middle: analyzer oriented horizontal, right: analyzer at 45°. The bright central spot is due to the infrared laser light.

the 5000th, i. e. after 5 seconds, using a photomultiplier. The oscilloscope traces of these two signals are depicted in Fig. 5.5. They are nearly identical, thus parametric scattering processes can be clearly excluded.

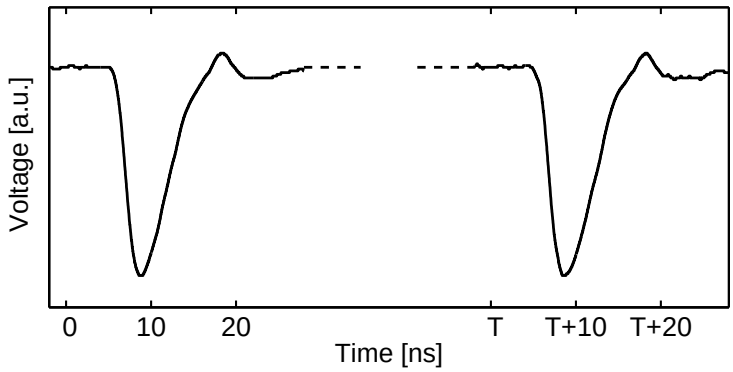

Figure 5.5: Oscilloscope traces of the ring intensity (photomultiplier signal) at the first and at the 5000th pulse of the exciting laser. The pulse width is approximately 5 ns, the time T between the two pulses shown here is 5 seconds.

Several authors have demonstrated that micrometer-sized needlelike domains play an important role for light scattering and for the type of the phase transition in SBN [50–53]. These domains are in antiparallel order, the ferroelectric polarization is parallel or antiparallel to the crystallographic c-direction. To prove whether these domains also are responsible for the non-collinear second-harmonic process, we poled a sample by cooling it down from the high-temperature paraelectric phase with an electric field applied in c-direction. After that no indication of a ring structure could be detected. That means that antiparallel ferroelectric domains are the basic cause for the non-collinear SHG effect, a

model has to be based on this fact.

5.2 The Model

A model to explain the second harmonic generation in SBN must be in agreement with the described observations and of course with the crystal particularities:

- Strontium Barium Niobate (SBN) has a small birefringence.
- For an incidence along the c axis the observed SHG ring is weak in poled and strong in un-poled samples.
- The intensity distribution in case of normal incidence regarding the crystals c-axis is homogeneous in as-grown samples but in case of poling the intensity is mainly distributed around 0° and 180° to the direction of the laser beam.
- while turning the crystal from the geometry with the laser beam parallel to the c-axis to the situation of the laser beam perpendicular to the c-axis the projected SHG image on a screen will change from Circle → Ellipse → Hyperbola → Straight line.
- The observed ring is radially polarized.
- The generation of the second harmonic must be in agreement with the d-tensor for SBN.

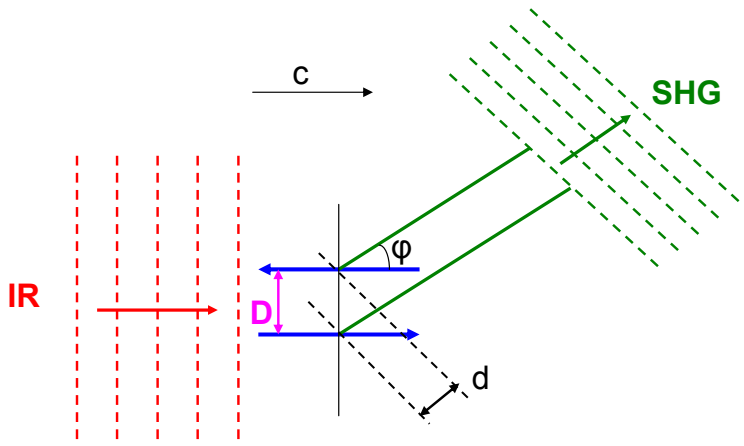

Figure 5.6: Schematic of two dipoles excited by the incoming infrared light wave and constructively interfering under a certain angle φ to build an SHG plane wave. D is half of the spatial periodicity for the domain distribution. d is the additional optical path for phase compensation.

The well defined SHG light pattern observed in the case of the SBN crystal strongly indicates that there must be phase matching; otherwise just a diffuse, homogeneously distributed, second harmonic light would be seen.
As a starting point we consider the simplest case, two antiparallel domains which are excited by an infrared wave as shown in Fig 5.6. Second harmonic polarization is induced via the tensor elements d_{31} and d_{32}. Due to the antiparallel direction of the ferroelectric polarization a phase shift of π results between the two second harmonic polarizations. The two domains thus can be regarded as dipole point sources for second harmonic radiation with a phase shift of π. Both, the dipolar radiation geometry and this phase shift prevent second harmonic radiation in forward direction, i.e. parallel to the infrared beam. The phase shift is compensated for directions where d is an odd multiple of $\lambda/2$, λ is the second harmonic wavelength.
In nonlinear optics problems like phase matching or quasi phase matching are treated most often not in the real space (wavelength description λ) but in the reciprocal space (momentum space k).
The periodicity of the antiparallel domains can be regarded as a grating. In the momentum space this will have a certain grating vector $\mathbf{K}_\mathrm{g}$. Then the phase matching condition (Fig. 5.12), described above in terms of λ, can be expressed in the momentum space like in Eq. 5.1

$$\mathbf{k}_\mathrm{SHG} = 2\mathbf{k}_\mathrm{IR} + \mathbf{K}_\mathrm{g} \tag{5.1}$$

with $|\mathbf{K}_\mathrm{g}|$ of the form:

$$K_\mathrm{g} = \frac{2\pi}{2D} \tag{5.2}$$

with $2D$ the periodicity of the domains.

If one considers the case of collinear quasi-phase matching, the momentum conservation is also like in Eq. 5.1, the only difference is that in this case all three vectors are collinear, thus this expression is true in a scalar sense. In our case the Eq. 5.1 is only true in a vectorial sense.
In the case of collinear quasi-phase matching the origin of the $\mathbf{K}_\mathrm{g}$ vector is evident, it comes from the periodically poling of the crystal. In our case it comes from the random distribution of the antiparallel domains. Thus the $\mathbf{K}_\mathrm{g}$ vectors from Eq. 5.1 are always contained in the (c)-plane.
For a better understanding of the link between the domain distribution in the crystal and the equivalent density of $\mathbf{K}_\mathrm{g}$ vectors in the momentum space it is useful to consider the following examples.

For the case of just two antiparallel dipoles sketched in Fig. 5.7*(left)* the density of states of the $\mathbf{K}_\mathrm{g}$ vectors in the momentum space will be like in Fig. 5.7*(right)*. That is a broad distribution of $\mathbf{K}_\mathrm{g}$ vectors with the maximum at the value corresponding to the period of

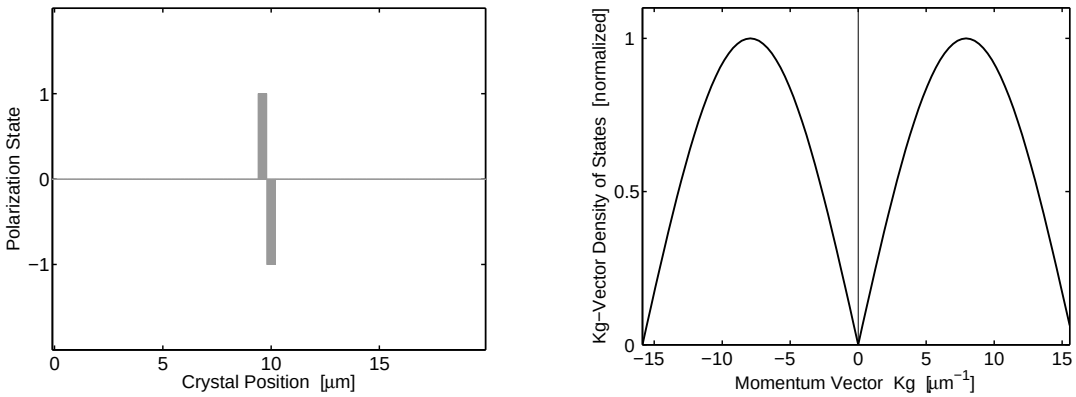

Figure 5.7: On the left two antiparallel dipoles in the real space are presented. On the right, in the momentum space, the corresponding distribution of the $\mathbf{K}_g$ vectors is shown. The maximum of the distribution corresponds to the spatial period of the dipoles.

the dipoles.
In the real space that will be also a rather broad angular intensity distribution as sketched in Fig. 5.8.

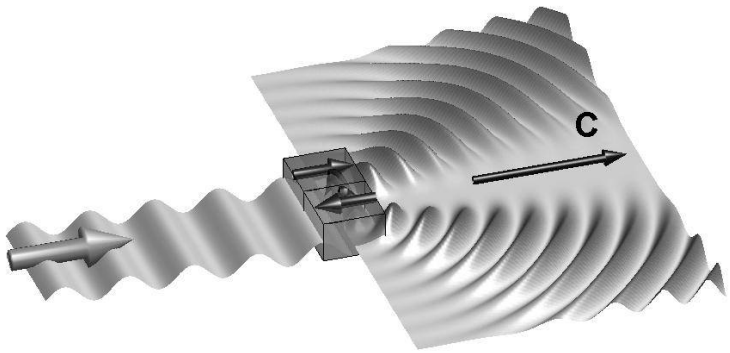

Figure 5.8: Angular distribution of the second-harmonic radiation originating from two antiparallel domains in SBN. The exciting wave propagates in c-direction from the left side.

While considering not just two antiparallel dipoles but a series of such dipole pairs the grating is more evident and also the distribution is very narrow with a maximum defined by the periodicity of the grating (Fig. 5.9).
We finally consider the case of a random distribution of antiparallel dipoles (antiparallel domains) what is most plausible case in a crystal. The result in the momentum space will lead to a continuous distribution of density of states of $\mathbf{K}_g$ vectors. If the randomness is getting higher then the distribution in the momentum space is getting closer to a homogeneous distribution of all states of $\mathbf{K}_g$ vectors (Fig. 5.10). Thus, in a crystal, one can expect

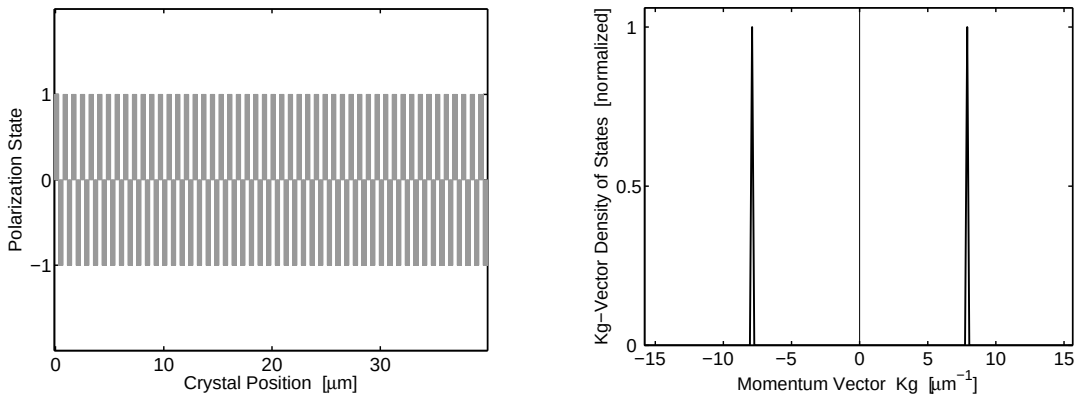

Figure 5.9: On the left, in the real space, a series of antiparallel dipoles with fixed periodicity are presented . On the right, in the momentum space, the corresponding, narrow, distribution of the $\mathbf{K}_\mathrm{g}$ vectors is shown. The maximum of the distribution corresponds to the spatial period of the dipoles.

a large variety of $\mathbf{K}_\mathrm{g}$ vector sizes. This was confirmed experimentally by the piezoelectric microscopy measurement reported by Kleeman et al. [53,54]. Fig. 5.11 is presenting a typical result of such a microscopy measurement. With dark and white regions are presented domains of opposite orientations. The image corresponds to (c)-plane, $100\mu m \times 100\mu m$ of an SBN sample. Due to the fractal-like shape of the domains a homogeneous distribution of the states in the momentum space is to be expected.

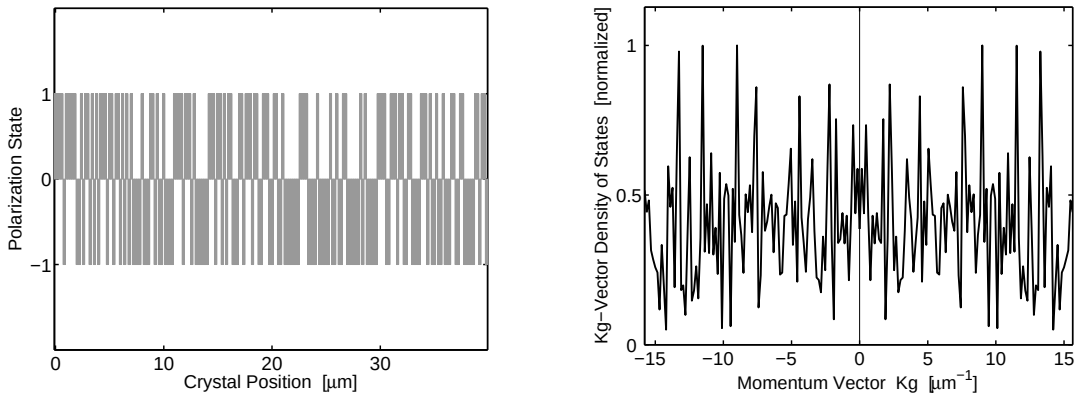

Figure 5.10: On the left, in the real space, a series of antiparallel dipoles with different sizes and thus different periodicity are presented. On the right, in the momentum space, the corresponding, almost homogeneous, distribution of the $\mathbf{K}_\mathrm{g}$ vectors is shown.

In the above examples always just one of the crystallographic directions a or b was considered. In reality have to deal with a two-dimensional distribution of the $\mathbf{K}_\mathrm{g}$ vectors in

the (c)-plane. It is not difficult to extend the conclusions from the uni-dimensional examples to the real two-dimensional case. In the two-dimensional fractal structure presented in Fig. 5.11 one can see that each particular direction in the (c)-plane will present the same properties from the point of view of the randomness. Thus in the real crystal a two-dimensional homogeneous distribution of $\mathbf{K}_g$ vector density of states can be expected. For this reason the obtained SHG-patterns have a much higher symmetry than the four-fold crystallographic one.

In a poled sample there are no more antiparallel domains, there is no more fractal structure of the domains and, of course, no more grating or long enough $\mathbf{K}_g$ vectors to fulfill the momentum conservation. Due to this fact is not possible to see any SHG ring in such a sample.

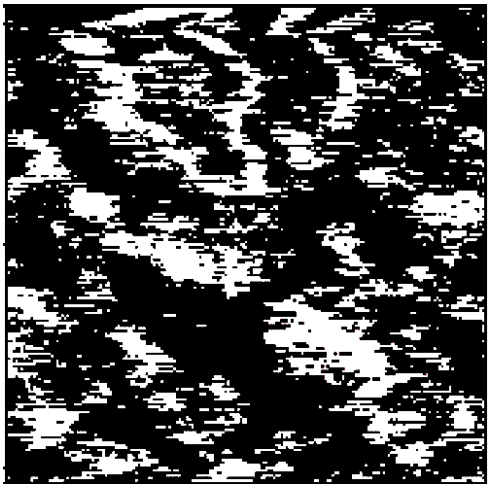

Figure 5.11: (c)-plane piezoelectric domain spectroscopy in an SBN crystal ($100\mu m \times 100\mu m$) [53, 54]. Black and white are different orientations of the ferroelectric dipoles. This picture shows a fractal-structure of the domains and domain borders.

In the very general case of a certain angle α between the incoming infrared light beam and the c-axis of the crystal the vectorial draw looks like in Fig. 5.12. The opening angle φ is related to α by the formula:

$$k_{\mathrm{SHG}} \cos(\varphi) = 2k_{\mathrm{IR}} \cos(\alpha) \tag{5.3}$$

Because all dipoles in the crystal are oriented parallel with the crystallographic c-axis one can conclude that the emitted SHG light is always symmetric with respect to the crystallographic c-direction. That means if one projects the SHG light on a screen perpendicular to the c-axis for different incident angles of the laser, α, the image will always be a circle of different radius.
The smallest radius of the SHG ring Fig. 5.3 *(right)* can be achieved with the geometry of

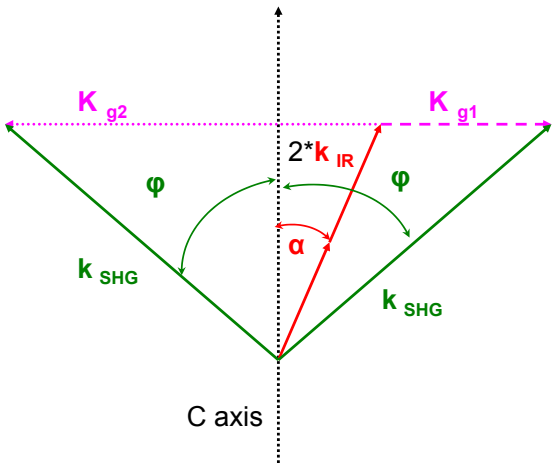

Figure 5.12: The momentum conservation in the general case with an angle α between the infrared light beam and the crystallographic c-axis. $\mathbf{k}_{\mathrm{IR}}$ and $\mathbf{k}_{\mathrm{SHG}}$ are the light k vectors for the infrared and the second harmonic. The vertical dashed line shows the crystallographic c-axis. $\mathbf{K}_{\mathrm{g}(1)}, \mathbf{K}_{\mathrm{g}(2)}$ are the grating vectors fulfilling the conservation relation.

the incident laser beam parallel to the crystallographic c-axis. In this case all $\mathbf{K}_{\mathrm{g}}$ vectors, fulfilling the momentum conservation, have the same length but different orientations. For each point of the SHG ring a particularly oriented $\mathbf{K}_{\mathrm{g}}$ vector will close the momentum triangle.
If the angle between the infrared laser beam and the c-axis of the crystal will be 90° ($\alpha = 90°$), Fig. 5.1 *(left)*, then the opening angle of the SHG cone Fig. 5.3 *(left)* $2 \times \varphi$ will be 180° and the cone will degenerate in to an SHG plane Fig. 5.1 *(right)*. For different directions the momentum conservation will be fulfilled with the help of specific $\mathbf{K}_{\mathrm{g}}$ vectors. The shortest $\mathbf{K}_{\mathrm{g}}$ vector will be involved in the forward harmonic generation. The longest vector will fulfill the momentum conservation for the backward second harmonic generation.
The homogeneous distribution of the SHG light intensity, under any angle between the forward and the backward generation, observed in the as-grown samples is a confirmation of the homogeneous distribution of the density of states of the $\mathbf{K}_{\mathrm{g}}$ vectors in the (c)-plane. After poling the sample this distribution will no longer be homogeneous, the domains will increase in size and the small domains will disappear. That means that the number of the short $\mathbf{K}_{\mathrm{g}}$ vectors will increase and the number of the long ones will decrease. Thus a high intensity in the forward direction can be seen and in the same time just a very week SHG light intensity can be observed for other directions Fig. 5.2.

In both pictures Fig. 5.1 *(right)* and Fig. 5.3 *(right)* one can see that the SHG light patterns have a certain width, i.e. fact there is a divergence of the second harmonic light. Up to this point all description of the SHG process was made considering the two-dimensional crystal,

always just a distribution of the $\mathbf{K}_g$ vectors in the (c)-plane was considered. The real crystal is in fact a three-dimensional system. All the domains involved in the second harmonic generation have a certain length along the c-axis. A limited length of the ferroelectric domains in real space will lead to a momentum vector component $\mathbf{K}_c$ parallel to the c-direction in reciprocal space. This vector $\mathbf{K}_c$ will also play a role in the momentum conservation. The final expression of the momentum conservation can be obtained by considering also this $\mathbf{K}_c$ vector in equation 5.1

$$\mathbf{k}_{SHG} = 2\mathbf{k}_{IR} + \mathbf{K}_g + \mathbf{K}_c \tag{5.4}$$

The two *domain vectors* $\mathbf{K}_g$ and $\mathbf{K}_c$ are always perpendicular to each-other. $\mathbf{K}_g$ is contained in the (c)-plane while $\mathbf{K}_c$ is along the crystallographic c-axis. The *action* of the $\mathbf{K}_c$ vector can be seen in a certain divergence of the SHG light. For a better understanding one can use again simple examples making the links between real and momentum space.

In the case of short domains Fig. 5.13*(left)* the resulting distribution of the $\mathbf{K}_g$ and $\mathbf{K}_c$ vectors are presented in Fig. 5.13*(right)*. A darker area of the image corresponds to a higher density of the $\mathbf{K}$ vectors.
For this situation a very pronounced divergence of the generated second harmonic light would be expected.

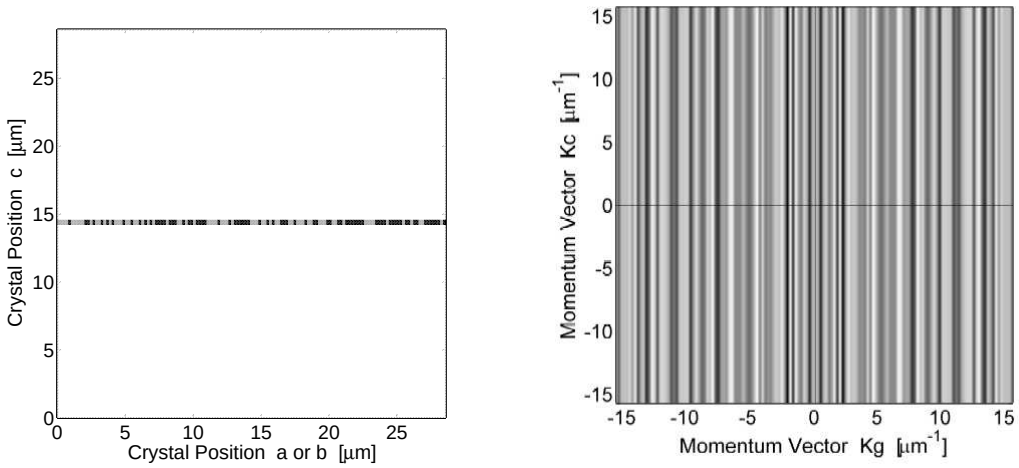

Figure 5.13: On the left, in real space, antiparallel dipoles (domains) with different sizes in the (c)-plane (a, b positions) are presented. The dark and gray regions represents opposite polarization states. In this example all domains are short (along the c-axis). On the right, in the momentum space, the corresponding distribution of the $\mathbf{K}_g$ and $\mathbf{K}_c$ vectors is presented. Due to the fact that the domains are short one can experience a large variety of $\mathbf{K}_c$ vectors. In this case a high divergence of the SHG light would be the result.

In the Fig. 5.14*(left)* long ferroelectric domains are considered, in this case the result in the momentum space Fig. 5.14*(right)* will lead to short $\mathbf{K}_c$ vectors. If this would be the case in the crystal, almost no divergence of the SHG light could be seen.

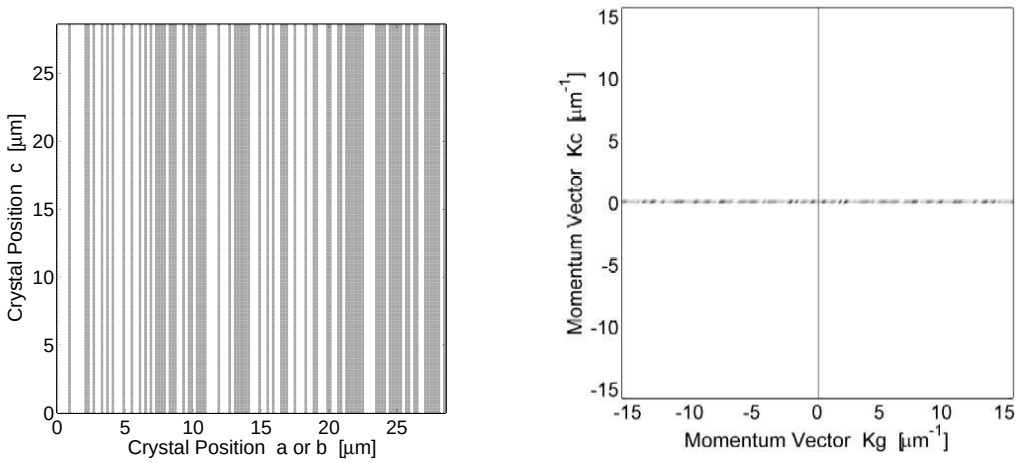

Figure 5.14: On the left, in real space, antiparallel dipoles (domains) with different sizes in the (c)-plane (a, b positions) are presented. The dark and gray regions represents opposite polarization states. In this example all domains are long (along the c-axis). On the right, in the momentum space, the corresponding distribution of the $\mathbf{K}_g$ and $\mathbf{K}_c$ vectors is shown. Due to the fact that the domains are long one can experience only short $\mathbf{K}_c$ vectors. In this case almost no divergence of the SHG light would be the result.

Of course the situation of medium length of the domains Fig. 5.15*(left)* will lead in the momentum space to a certain maximum length of the $\mathbf{K}_c$ vectors Fig. 5.15*(right)*. For this situation one would experience a certain divergence of the SHG light. The maximum of this divergence is given by the longest $\mathbf{K}_c$ vectors.

The closest example to the real situation in the case of the SBN crystal is presented in Fig. 5.16*(left)*. In this case stripes of medium length domains along the crystallographic c-axis are considered. The crystal would not exhibit such a perfect periodicity of the domain lengths as not all domains from a certain stripe would have the same length. One can learn from this example that in momentum space by such a distribution of domains a maximum length of the $\mathbf{K}_c$ vectors will determine a divergence of the generated SHG light.
In the real crystal one can associate the longest $\mathbf{K}_c$ vectors with the shortest domains. Thus while carefully measuring the divergence of the SHG light it is possible to determine the minimum length of the ferroelectric domains. Measurements of this type revealed that in SBN crystal the domains are longer than 20 μm. That confirms the long needle-like domains reported in the literature [50–53] in the case of this crystal.

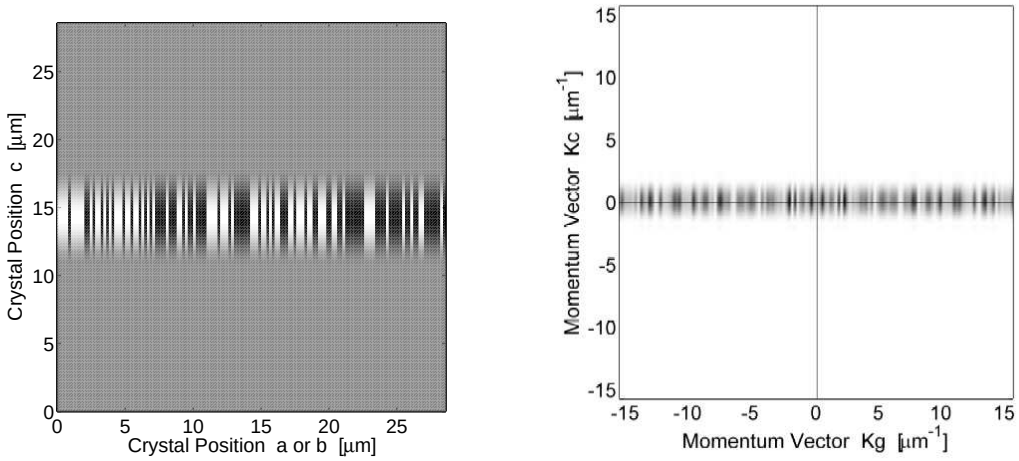

Figure 5.15: On the left, in real space, antiparallel dipoles (domains) with different sizes in the (c)-plane (a, b positions) are presented. The dark and gray regions represents opposite polarization states. In this example medium length domains (along the c-axis) are presented. On the right, in the momentum space, the corresponding distribution of the $\mathbf{K}_{\mathrm{g}}$ and $\mathbf{K}_{\mathrm{c}}$ vectors is shown. The length of the domains will determine a maximum length of the $\mathbf{K}_{\mathrm{c}}$ vectors. In this case a maximum of divergence is given by the longest $\mathbf{K}_{\mathrm{c}}$ vectors.

5.3 Ring Properties

Two experiments have been made to verify the Domain Induced Second Harmonic Generation (DISHG) model. In the first experiment the angle between the infrared laser light and the direction of the crystallographic c axis, α, has been changed. By measuring the diameter of the SHG ring on the projection screen one can calculate the cone angle φ. From the diagram of the momentum conservation in Fig. 5.12 the relation between the angles α and φ can be extracted.

$$2 \times k_{\mathrm{IR}} \cos(\alpha) = k_{\mathrm{SHG}} \cos(\varphi) \tag{5.5}$$

or written in terms of refractive indices

$$n_{\mathrm{IR}}(ord) \cos(\alpha) = n_{\mathrm{SHG}}(\varphi) \cos(\varphi) \tag{5.6}$$

with $n_{\mathrm{SHG}}(\varphi)$ of the form:

$$n_{\mathrm{SHG}}(\varphi) = \sqrt{\frac{n^2_{\mathrm{SHG}}(ord) n^2_{\mathrm{SHG}}(ext)}{n^2_{\mathrm{SHG}}(ext) \cos^2(\varphi) + n^2_{\mathrm{SHG}}(ord) \sin^2(\varphi)}} \tag{5.7}$$

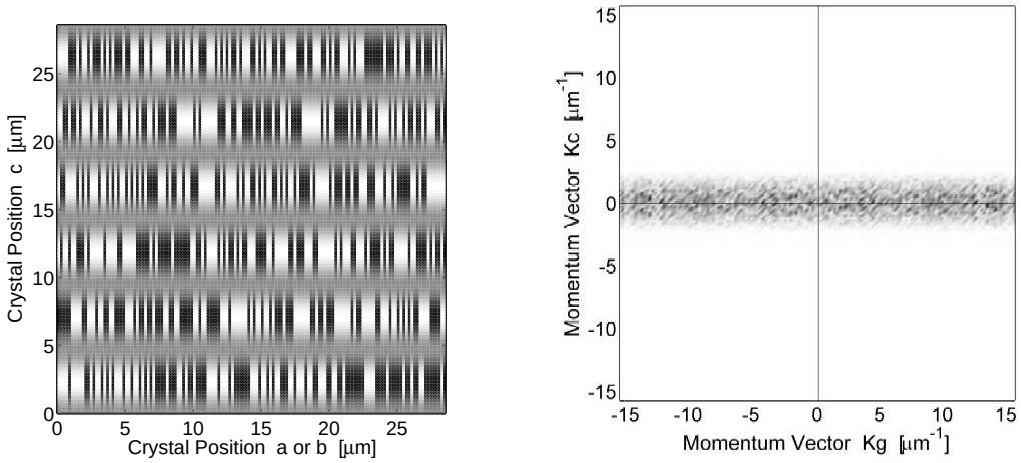

Figure 5.16: On the left, in real space, antiparallel dipoles (domains) with different sizes in the (c)-plane (a, b positions) are presented. The dark and light regions represents opposite polarization states. In this example stripes of medium length domains (along the c-axis) are presented. On the right, in the momentum space, the corresponding distribution of the $\mathbf{K}_\mathrm{g}$ and $\mathbf{K}_\mathrm{c}$ vectors is shown. The length of the domains will determine a maximum length of the $\mathbf{K}_\mathrm{c}$ vectors. In this case a maximum of divergence is given by the longest $\mathbf{K}_\mathrm{c}$ vectors.

5.3.1 Angle Dependence

The experimental setup sketched in Fig. 5.17 uses an infrared Nd:YAG pulse laser. The SBN crystal is placed on a rotating table with the c-axis oriented perpendicular to the projection screen. A camera situated behind this screen records images of the second harmonic ring. The screen, the camera and the crystal can be turned by an arbitrary angle. In this way the angle between the laser and the c-axis of the crystal can be varied. The results of this measurement are shown in Fig. 5.18. It presents the angle φ as a function of the angle α_A (the angle α in air). The continuous line is the one obtained from the model according to Eq. 5.5 and the dots are the experimental results. The largest error between the experimental results and the theoretical calculation does not exceed 1°. This error can be referred to either a systematic error while turning the table with the crystal, misalignment of the projection screen regarding the crystal c-axis or to approximations made during the evaluation of the data.

5.3.2 Wavelength Dependence

For the second measurement a tunable dye laser has been used to generate infrared light with different wavelengths. In this case the angle α_A between the laser light and crystallographic c axis of the SBN was fixed to $\alpha_\mathrm{A} = 0°$. While changing the wavelength of the

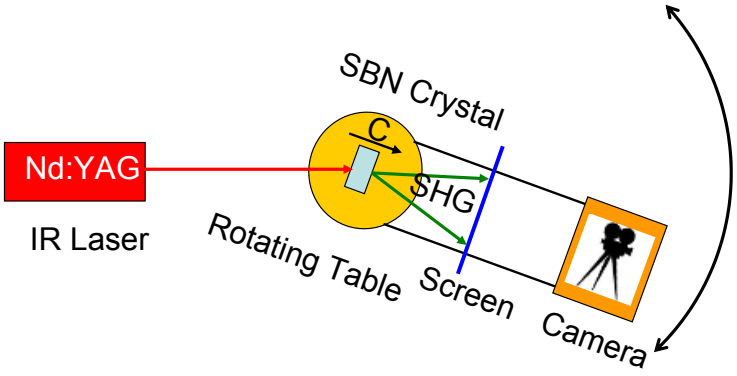

Figure 5.17: Angle dependence experimental setup for verifying the domain induced second harmonic generation model in SBN: On the left side is a Nd:YAG infrared laser which is illuminating the SBN crystal. The second harmonic image is projected on a screen. A camera on the right side records images for different angles of the rotating table.

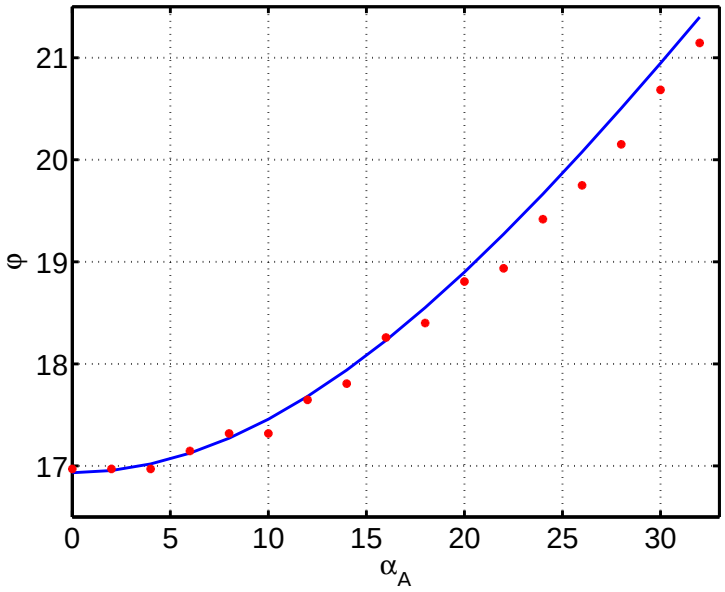

Figure 5.18: Comparison between the theoretical and experimental dates for the measurements with different incident angle of the laser beam α_A. The continuous line represents the theoretical calculations and the dots are experimental results.

laser, the length of the momentum vector $\mathbf{k}_{IR}$ for the infrared light was altered resulting in the change of the cone angle. The experimental setup for this measurement is shown in Fig. 5.19

Also in this case the agreement between the experimental results and the calculation was

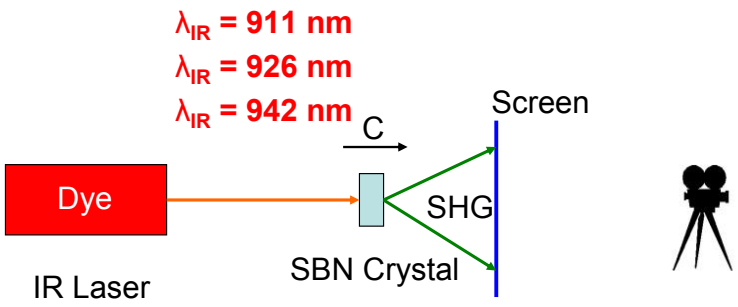

Figure 5.19: The wavelength dependence experimental setup. Developed to check the domain induced second harmonic generation model in SBN. On the left side is a tunable infrared dye-laser which is illuminating the SBN crystal. The second harmonic image is projected on a screen. A camera situated on the right side of the figure records this images for different wavelengths of the dye-laser.

very good. In Fig. 5.20 the cone angle φ as a function of the wavelength of the dye-laser is presented. The solid line is the dependence calculated from Eq. 5.5 and the dots are again the experimental values. The errors are less than half degree and could come from misalignments or corrections which were applied due to particularities of the crystal holder.

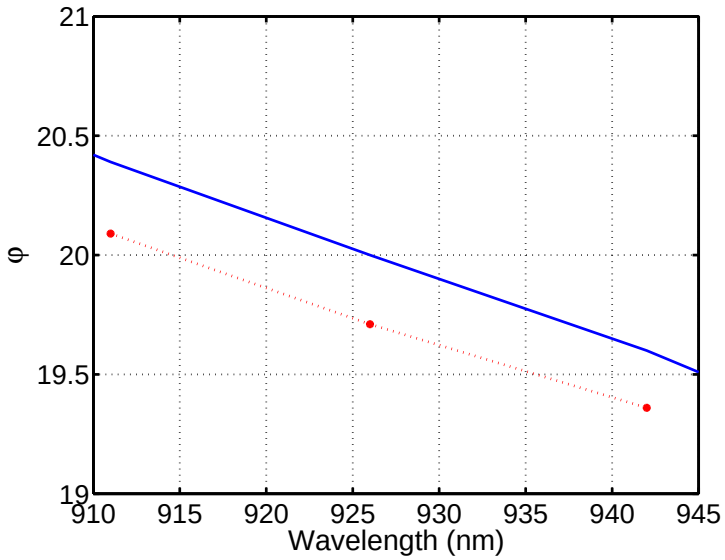

Figure 5.20: Comparison between the theoretical and experimental dates for the measurements with different incident wavelengths of the laser beam. The continuous line represents the theoretical calculations and the dots are experimental results.

5.4 Applications of Radially Polarized Light

Domain induced non-collinear second harmonic generation is a new nonlinear process of general fundamental interest. In addition, it provides a practically ideal source of radially polarized light which may lead to interesting applications. Two of these potential applications will be briefly sketched here.

5.4.1 Focusing

The spatial resolution of optical instruments like microscopes is usually limited by the smallest focus spot achieved. This limit is governed by diffraction present everywhere in optical systems. Several authors, yet, have shown [8–12] that the limit, i.e. the smallest spot size, also depends sensitively on the polarization state of the light. Using Maxwell's equations which are symmetric in time and studying the case of the light emission by an elementary dipole, Quabis et al. [8–10] have proved that the best focusing can be done for a light pattern having the same symmetry as the one of the radiation emitted by the elementary dipole. It is known from electrodynamics that the symmetry of the radiation emitted by an oscillating dipole is a circular one. The intensity distribution is a toroid centered on the dipole axis (Fig. 5.21).
If this emission process is time-reversed, it can be shown that the distribution of the light pattern can collapse to the atomic dimensions.

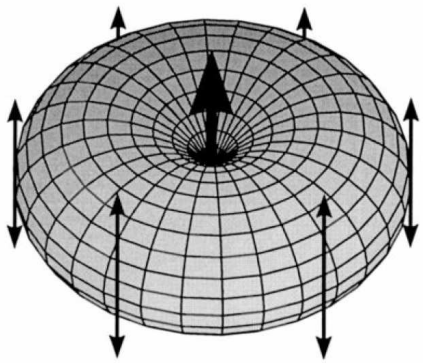

Figure 5.21: The 2D-polar plot of an oscillating dipole. The dipole emits mainly in the direction perpendicular to its axis with polarization indicated by the thin arrows parallel to the dipole axis. To achieve a small focused spot, the electric field in the image space should be similar to the time-reversed field.

If one analyzes the symmetry of the light distribution in the focus of a lens for different polarization states it can be shown that only the pattern of the radially polarized light has the same rotational symmetry as that of the elementary dipole. In this case the polarization vector of the focused light is parallel to the optical axis (Fig. 5.22 *right*), like in the case

of the polarization of a dipole radiation which was parallel with the dipole axis. If one -in contrast- considers the case of linearly polarized light then the electric vector of the light will be perpendicular to the optical axis (Fig.5.22 *left*).

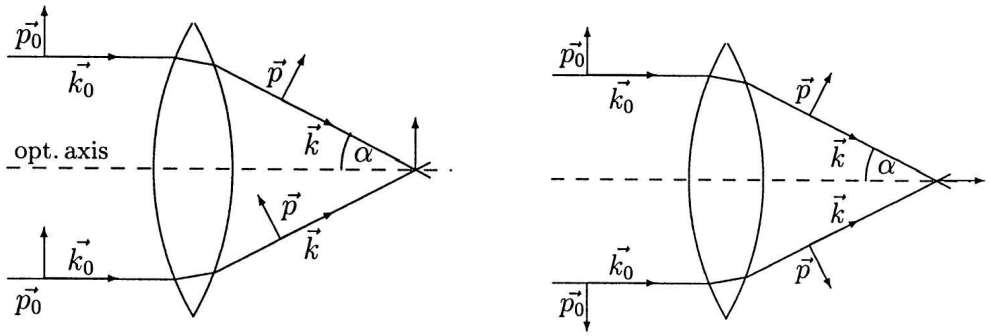

Figure 5.22: Polarization of the focused light in the case of: *left* linearly polarized incident light and *right* radially polarized incident light.

The energy distribution in the focal plane for the two cases is shown in Fig. 5.23

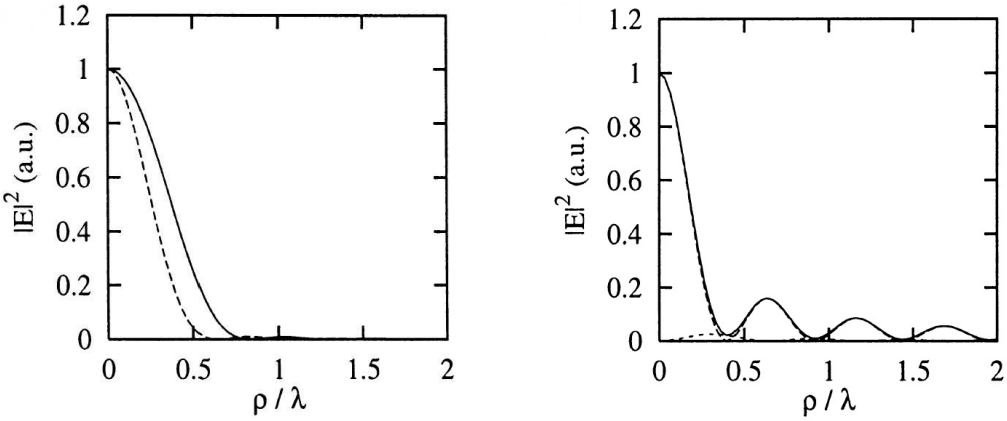

Figure 5.23: The energy distribution in the focus plan for: *left* the linearly polarized light and *right* the radially polarized light. In the case of radiall polarization the energy is focused inside a circle with radius ρ smaller than half the wavelength of the light.

One can observe that in the case of the radially polarized light the energy can be better focused than for a linearly polarized beam. This particularity may be of importance in applications like Laser Scanning Confocal Microscopy where the scanning resolution is strongly dependent on the laser light focusing.

5.4.2 Cylindrical Polarization

Radial polarization is a special case of cylindrical polarization. From a theoretical point of view cylindrically polarized light states are of great interest, as due to their symmetry they facilitate calculations.
Using two half-wave plates, a radially polarized beam can be transformed into any cylindrically polarized state as shown in the following. Using two half-wave plates with an angle γ between each other's fast axis, any incoming polarization vector of a light beam will be turned by an angle $2 \times \gamma$. If $\gamma = 45°$, the polarization vector of the out-going light beam will be rotated by 90° compared to the direction of the incident polarization.
Let us consider a cartesian system with axis **X** and **Y** using the following notations: P_x and P_y are the polarization components of the incoming light, P'_x and P'_y the polarization components of the light after passing the system of two half-wave plates. γ is the angle between the two plates. For simplicity we can choose the first half-wave plate oriented with its axis in the same direction as the cartesian coordinate axis **X**. The Jones matrix for this half-wave plate is of the form:

$$\begin{pmatrix} 1 & 0 \\ 0 & -1 \end{pmatrix} \tag{5.8}$$

The second half-wave plate is rotated by the angle γ. To describe the action of this plate, the polarization status after the first plate need to be turned by an angle $-\gamma$ to the eigen system of this plate. Finally a second turning with angle γ will restore the coordinates to the considered cartesian system. If $R(\gamma)$ and $R(-\gamma)$ are the rotation matrices, then the polarization of the light after the two plates is of the form:

$$\begin{pmatrix} P'_x \\ P'_y \end{pmatrix} = R(\gamma) \begin{pmatrix} 1 & 0 \\ 0 & -1 \end{pmatrix} R(-\gamma) \begin{pmatrix} 1 & 0 \\ 0 & -1 \end{pmatrix} \begin{pmatrix} P_x \\ P_y \end{pmatrix} \tag{5.9}$$

With $R(\gamma)$ of the form:

$$R(\gamma) = \begin{pmatrix} \cos(\gamma) & -\sin(\gamma) \\ \sin(\gamma) & \cos(\gamma) \end{pmatrix} \tag{5.10}$$

The result is of the form:

$$\begin{pmatrix} P'_x \\ P'_y \end{pmatrix} = \begin{pmatrix} \cos^2(\gamma) - \sin^2(\gamma) & -2\cos(\gamma)\sin(\gamma) \\ 2\cos(\gamma)\sin(\gamma) & \cos^2(\gamma) - \sin^2(\gamma) \end{pmatrix} \begin{pmatrix} P_x \\ P_y \end{pmatrix} \tag{5.11}$$

and this can be written as:

$$\begin{pmatrix} P'_x \\ P'_y \end{pmatrix} = R(2\gamma) \begin{pmatrix} P_x \\ P_y \end{pmatrix} \tag{5.12}$$

Light with an azimuthal polarization has a high symmetry and thus is preferred by theoretical physicists for model calculation of waveguides, optical fibres etc. From the second harmonic of the SBN crystal it is easy to obtain this polarization state and thus sources

of azimuthally polarized light can be easily made available for experimentally checking the model calculations.

Chapter 6

Second Harmonic Generation as a Tool

6.1 Experimental Setup

The experimental setup is shown in Fig. 6.1. A Nd:YAG infrared laser is illuminating the SBN crystal. Four photomultipliers, situated at 0, 45, 90 and 135 degree with regard to the direction of the laser light, record the generated second harmonic. Using a heater the temperature of the crystal can be adjusted in a range from 0 to 300 centigrade with a resolution of 0.1°.

6.2 Determination of the Phase Transition Temperature

Like in the case of the known non-collinear harmonic generation schemes also the domain induced second harmonic generation (DISHG) can be used to determine certain parameters of the crystal, perhaps the most important is the temperature of the ferroelectric - paraelectric transition.

6.2.1 Introduction

At room temperature the SBN crystal is in a ferroelectric phase with the point group 4 m m [3, 4, 24, 55–57]. At higher temperatures, depending on the Strontium - Barium ratio, a phase transition will bring the crystal to a paraelectric phase with the point group 4/m m m. Several works known in the literature were done to study the phase transition of SBN crystals [54, 58–61]. It is difficult to define an exact temperature of the phase transition as the material shows strong relaxor properties especially for the Strontium rich compositions. Therefore, as a parameter of the phase transition, a Curie region instead of

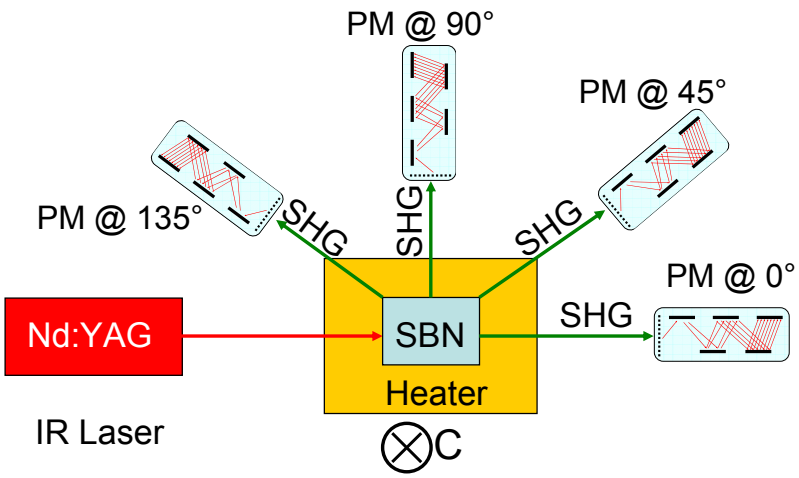

Figure 6.1: Sketch of the experimental setup used to SHG-determine the phase transition temperature of the SBN crystal. On the left side of the image an infrared Nd:YAG laser is shown illuminating the crystal. The sample is situated on a thermo-controlled plate which can fix the temperature with an accuracy of 0.1° in a range from 0° up to 300°. Four photomultipliers are recording the second harmonic signal at different angles as a function of the crystal temperature.

a distinct Curie temperature must be defined [19,20,62]. On the other hand it is not very convenient to speak about a temperature region when refering to the phase transition of such a relaxor material. Therefore usually a distinct temperature is chosen to express the transition. The way of defining this distinct transition temperature is not always the same. In all ordered materials the ordering can be expressed using an order parameter. For materials where the ordering interaction is an electric one for this parameter the polarization is used. In cases where the phase transition is of first order the order parameter can be expressed with a step function. In this case is very easy to define the phase transition temperature. In a second order phase transition, however, the order parameter will change continuously from a non-zero value to zero. In this case as a measure for the phase transition the temperature corresponding to the inflection point of the polarization change can be used [1,63,64]. Usually this temperature 'T_C' is not the center value of the Curie range, therefore also other temperatures can be chosen [19,64] to express the phase transition in some different way.

Authors like David, Granzow et al. [63] have determined phase transition temperatures directly from measurements of the inflection point of the temperature dependence of the spontaneous polarization. A different way to define the phase transition temperature uses measurements of the second harmonic intensity. In this case not the static (linear) polarization but the nonlinear polarization is measured.
As shown in the chapters dedicated to harmonic generation, the second order nonlinear

polarization is the source of second harmonic light. The relation between the fundamental laser light and the nonlinear polarization can be expressed using the the second order susceptibility tensor Eq. 3.16.
For the ferroelectric phase with pointgroup 4 m m the susceptibility d tensor has several nonzero components (Eq. 6.1 *left*). In the centro-symmetric phase the SBN crystal can be characterized by a pointgroup 4/m m m, this symmetry forces the d tensor to zero (Eq. 6.1 *right*).

$$\begin{pmatrix} 0 & 0 & 0 & 0 & d_{15} & 0 \\ 0 & 0 & 0 & d_{24} & 0 & 0 \\ d_{31} & d_{32} & d_{33} & 0 & 0 & 0 \end{pmatrix} \Leftarrow \text{phase transition} \Rightarrow \begin{pmatrix} 0 & 0 & 0 & 0 & 0 & 0 \\ 0 & 0 & 0 & 0 & 0 & 0 \\ 0 & 0 & 0 & 0 & 0 & 0 \end{pmatrix} \tag{6.1}$$

In other words, no more second harmonic light will be generated in the paraelectric phase of the crystal. Measuring the second harmonic intensity while the crystal is heated over its phase transition makes it possible to determine the temperature of the transition again using e.g. the inflection point.

6.2.2 Measurement and Results

A typical result of such a measurement is shown in figure 6.2. The upper part of the image presents the real measurement for a sample with a composition $x = 0.48$ (with x from $Sr_xBa_{1-x}Nb_2O_6$). The central part of the figure is the smoothed second harmonic curve recorded during the heating of the sample. To determine the inflection point of this curve the first derivative was calculated and is also plotted below on the same box. The negative maximum of the first derivative, the inflection point of the second harmonic curve, for heating has a value on the temperature scale at 139.5°. The lowest part of the same figure presents the cooling behavior. In this case the inflection point of the second harmonic curve is situated around 134°.

Figure. 6.3 shows a comparison between results of T_C obtained via pyro-electric and SHG measurements. One can see that there is a very good agreement between the results of the two measurements. For the pyro-electric measurements the samples were poled at high temperature (above the phase transition), in the case of the second harmonic measurements both as-grown samples and poled ones were used. There was no significant temperature shift between poled and unpoled measurements. All what could be regarded as temperature shift was in the range of the measurements error. Authors in the literature, however, as Granzow et al. [58] claim some significant temperature shift. An explanation to satisfy both observations will be presented in the last part of this chapter.
The advantage of the measurements using second harmonic generation in comparison with pyro-electric ones are evident if one considers that there is practically no interaction between the measurement device and the sample, so in this case the measured crystal is totally unperturbed by the measurement device. Thus a more precise investigation can

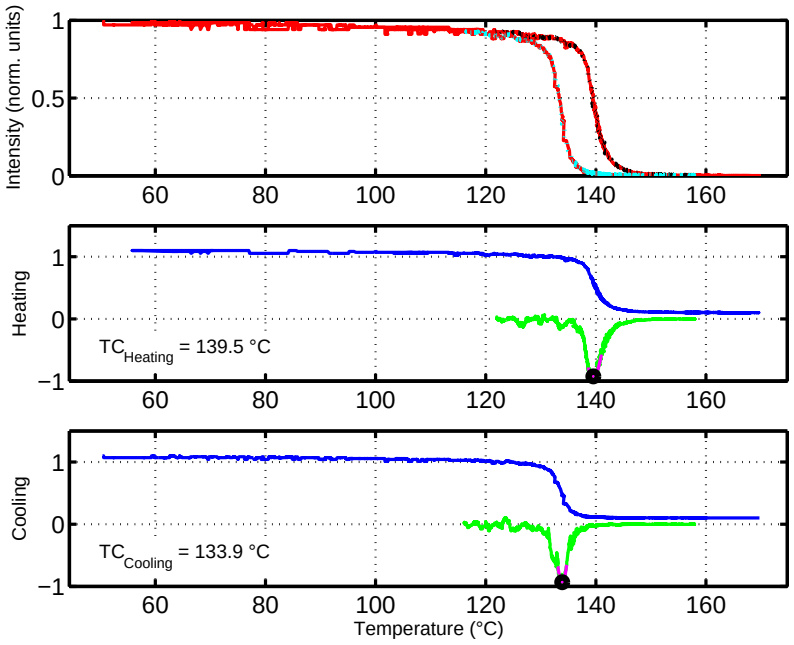

Figure 6.2: Typical result of SHG measurements for the determination of the phase transition temperature of a crystal with a composition $x = 0.48$. The upper curves are directly obtained from the measurement, the middle and lower are separately for heating and cooling. Also the first derivative is presented just around the phase transition.

be made. In the case of the pyroelectric measurements not just the interaction between the measurement setup and the crystal is the disadvantage but in all cases a poling of the sample is required and that will automatically set the crystal in a special, not as-grown, state.
Another disadvantage, in the case of SBN, of using the pyroelectric measurement consists in the fact that this crystal has a high conductivity for the Barium rich compositions which makes it practically impossible to pole these crystals.
A further advantage is the fact that for the determination of the phase transition using SHG measurements only a very small region of the bulk will be measured. Usually the infrared spot on the crystal is in the range of 50 - 200 μm. Thus results will come only from such a region. This potentially could be used for a topography of the sample.
It must be mentioned that in case of SHG measurements local thermal disorder can be induced in the crystal due to high focusing and thus important changes of the T_C value may be experienced. This is especially important for the composition ranges with high strontium content, due to low values of the d tensor of this crystals.

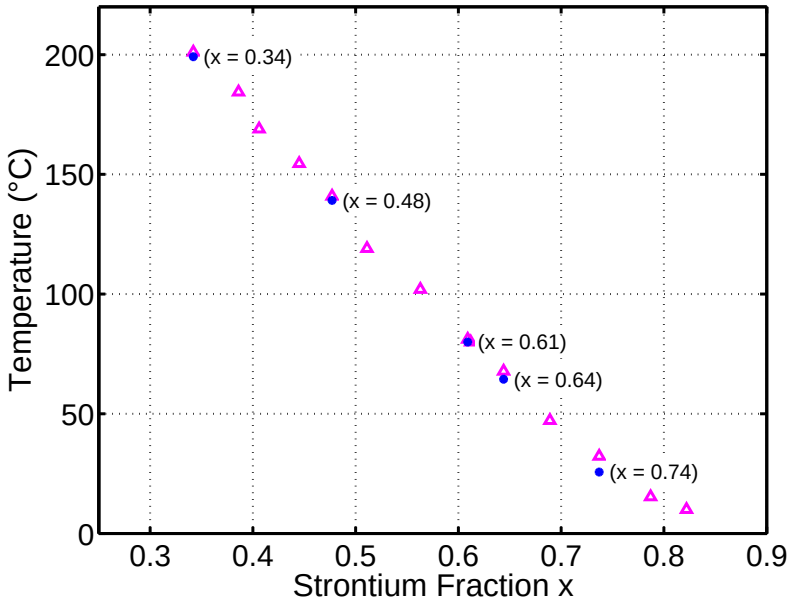

Figure 6.3: Result of phase transition temperature T_C determination with two methods. The circles are the results of pyro-electric measurements. The dots are values ,for some crystals with compositions shown in the brackets, obtained from SHG measurements.

6.2.3 Discussion

The decrease of T_C with increasing Strontium content qualitatively agrees with observations reported in the literature [1, 65]. However, the transition temperatures shown here deviate from the literature values: We observed higher T_C for small values of x and lower T_C for high values of x. A possible explanation lies in the uncertainty of the composition of the samples used for earlier studies, where generally only the Sr-content in the melt is given. In our measurements we used the Sr-content in the crystals as parameter. According to the solidus-liquidus phase diagram [21], the actual Sr-content x in the sample tends to shift closer to the congruently melting composition, $x = 0.61$. This explains the systematic deviation of our T_C from earlier literature values. Furthermore, the transition temperatures reported earlier stem from dielectric measurements and are less reliable due to their frequency-dependence [61, 66].

The nonlinear behavior of $T_C(x)$ can be explained by structure induced polarization changes. SBN belongs to the structure type of the tetragonal tungsten bronzes, i.e., the structure consists of corner-linked Nb_2O_6 octahedra forming pentagonal, tetragonal and trigonal channels [3, 67]. Because of the only Sr containing tetragonal channel and the strong variation of the Sr / Ba ratio in the pentagonal channel one can regard the compositional changes of $Sr_xBa_{1-x}Nb_2O_6$ as being caused by three sub-lattices. Sub-lattice (1) may be devoted to Sr in tetragonal sites, (2) to Sr in pentagonal ones, while (3) is devoted to Ba.

Within an effective field approach [68] the polarization of m coupled systems is described by m equations of the form:

$$P_i = N_i \mu_i \tanh\left(\frac{(E + x_i \beta_i P_i + \sum_{k \neq i}(x_k \alpha_{ik} P_k))\mu_i}{k_B T}\right) \tag{6.2}$$

The parameters α_{ik} describe the coupling strength between the subsystems with polarization P_i, the number of elementary dipoles N_i, the dipole moments μ_i and the effective fields β_i, while $k_B T$ has the usual meaning. The relative portions are x_i and $\sum_i x_i = 1$. For temperatures approaching T_C the polarization approaches zero, the hyperbolic tangent can be approximated by its argument. Summarizing several parameters in $T_i = \beta_i N_i \mu_i^2 / k_B$, which might be regarded as the Curie temperatures of the 'pure' sublattices, Eq. 6.2 transform to:

$$(a_{ki} - \delta_{k,i} T) P_i = b_i E_i \quad \text{with} \quad a_{ki} = \begin{cases} x_i T_i & \text{for } k = i \\ x_i T_i \alpha_{ki} / \beta_k & \text{for } k \neq i \end{cases}, \quad b_i = T_i / \beta_i \tag{6.3}$$

The polarizations should be able to approach any value at T_C at zero field. Therefore the determinant of the coefficients must vanish. For $m = 3$ we derive $T_\mathrm{C}^3 - s_2 T_\mathrm{C}^2 + s_1 T_\mathrm{C} - s_0 = 0$ with

$$s_2 = \sum_i a_{ii}, \quad s_1 = \sum_{i,k>i} (a_{ii} a_{kk} - a_{ik} a_{ki}), \quad s_0 = \sum_{i \neq k \neq l \neq i} \left(a_{i1} a_{k2} a_{l3} (-1)^{np(ikl)}\right) \tag{6.4}$$

and $np(ikl)$ is the number of permutations necessary to produce the index set $\{i, k, l\}$ from $\{1, 2, 3\}$. Because an exact solution is awkward to manage, we linearize the third order equation by substituting $s_2 + \Delta$ for T_C and omitting all nonlinear terms in Δ. Physically this is well justified as s_2 is the 'classical' Curie temperature, the weighted sum over the Curie temperatures of the 'pure' sublattices $s_2 = \sum_i a_{ii} = \sum_i (x_i T_i) = T_\mathrm{C}^{classical}$ and only minor deviations are expected. We obtain:

$$T_\mathrm{C} = s_2 + \frac{s_0 - s_1 s_2}{s_1 + s_2^2} \quad \text{with} \quad s_1 s_2 \gg s_0 \quad \text{and} \quad s_2^2 \gg s_1 \quad \text{and thus} \quad T_\mathrm{C} = s_2 - \frac{s_1}{s_2} \tag{6.5}$$

The parameter s_1 is a slightly more complex sum, but replacing the quotients $(\alpha_{ik}\alpha_{ki})/(\beta_i \beta_k)$ therein by an appropriate average factor λ^2 we arrive for the Curie temperature finally at:

$$T_\mathrm{C}(x_i) = T_\mathrm{C}^{classical} - \frac{1 - \lambda^2}{T_\mathrm{C}^{classical}} \sum_{i,k>i} (x_i x_k T_i T_k) \tag{6.6}$$

It must be pointed out that for a system with two sublattices, the parameter $(\alpha_{ik}\alpha_{ki})/(\beta_i \beta_k)$ reduces to $(\alpha_{12}\alpha_{21})/(\beta_1 \beta_2) = \lambda^2$ because of $\alpha_{12} = \alpha_{21}$ and thus Eq. 6.6 equals that in [69] after some appropriate linearizing.

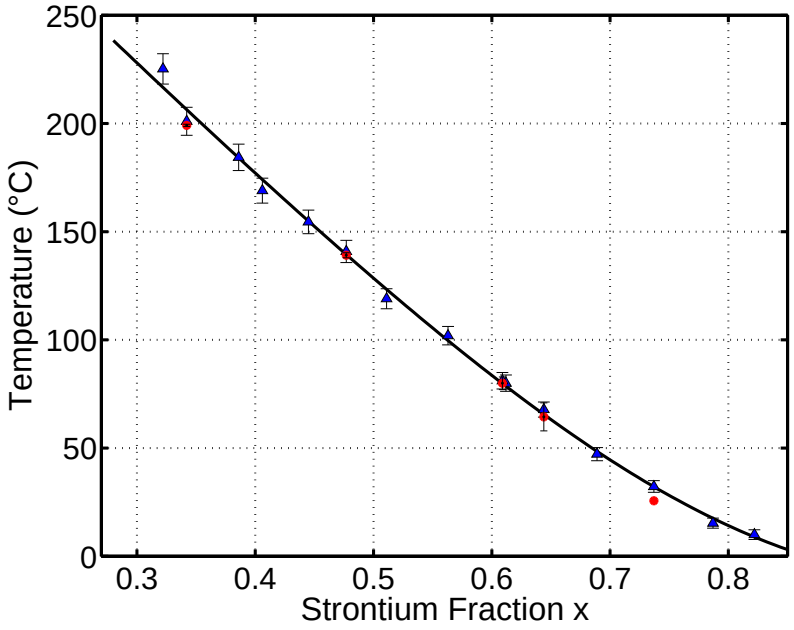

Figure 6.4: Temperature T_C for SBN in dependence on the Sr fraction x. The solid line represents the fit using equation 6.6, pyroelectric results are depicted with filled triangle. Solid dots are the results of SHG measurements.

In Fig. 6.4 the transition temperature T_C is presented as a function of the strontium fraction $x = x_1 + x_2$. For a fit of our data with equation 6.6 we took into account a constant contribution of Sr on tetragonal sites by setting $x_1 = 0.29$, which corresponds to about 72%, and $x_3 = 1 - x$. The fit yields $\lambda = 0.51$, $T_1^{tetr}(\mathrm{Sr}) = \mathrm{T}_2^{\mathrm{pent}}(\mathrm{Sr}) = 304$ K, and $T_3(\mathrm{Ba}) = 668$ K, respectively. Allowing $T_1^{tetr}(\mathrm{Sr}) \neq \mathrm{T}_2^{\mathrm{pent}}(\mathrm{Sr})$ simply results in an additional parameter without improving the quality of the fit. This means that constant polarization contributions like Sr on tetragonal sites or Niobium-Oxygen octahedra are implicitly included by an appropriate change of the temperature constants. Therefore the temperatures given should be regarded as fit parameters only. A λ less than 1 means that in this mixed system the coupling strength between the sub-lattices is weaker than the average value of the coupling strength within each sublattice. Such a reduction may be due to random internal strain fields in the crystal lattice introduced by the different ionic sizes of Sr and Ba.

6.3 Other results of the SHG measurements

Several further aspects of the phase transition can be analyzed using second harmonic measurements. In the experimental setup shown in figure 6.1 one can see that the generated harmonic is measured with four photomultipliers representing four different angles.

From the model of the second harmonic generation DISHG presented in the previous chapter we can derive that different angles corresponding to different $\mathbf{K}_g$ vectors for momentum conservation. Thus the intensity in each direction is proportional to the density of momentum vectors fulfilling the conservation relation for the considered direction. These measurements revealed that in as-grown samples the density of $\mathbf{K}_g$ vectors is a very homogeneous one. Independent of the composition of the sample, for a virgin crystal always practically equal intensity of the SHG is recorded in all directions. That means a 'perfect' fractal structure of the ferroelectric domains, the largest disorder, the highest entropy, for this state.

After applying electrical treatment to the sample the domain structure changes. Domains with a polarization in the same direction as the applied electric field will increase, those antiparallel to the field will decrease, small ones will even disappear. The domain borders will become more smoothed and thus the density of small $\mathbf{K}_g$ vectors becomes higher than the density of the large ones. This can be experimentally verified, after poling the sample no more homogeneous intensity distribution around the crystal is found. The emitted intensity of the second harmonic light increases in the forward direction, the direction corresponding to small $\mathbf{K}_g$ vectors. The light intensity measured with the photomultiplier situated at 90° decreases after the sample is poled. The virgin state of the crystal can be regained after slowly heating the sample over its phase transition. After cooling the homogeneous SHG intensity distribution can be observed as it was in the as-grown state. Figure 6.5 presents the SHG measurements for a congruent crystal ($x = 0.61$) after the sample was high temperature poled. The left graph was recorded using the photomultiplier situated at 90°. The measurements in the right graph are the results obtained with the central multiplier. The two curves in each graph represent the heating and the cooling measurements, respectively. For the measurement recorded with the photomultiplier situated perpendicular to the direction of the laser beam, the heating curve is the lower one, starting from an initial value of SHG intensity around 0.1 (normalized units). After the crystal is reaching its phase transition temperature the original, un-poled state is regained and one can see that for the cooling curve a much higher SHG intensity is obtained. The cooling curve terminates with an intensity around 0.9 (normalized units).
In the case of the data recorded using the forward photomultiplier the initial value of the SHG intensity is very much higher in the initial poled state of the crystal, the heating curve is the upper one in the *right* picture. The solid line is a Savitzky-Golay smoothed curve to the noisy data. In this case, after heating the sample over the phase transition, the final intensity of the second harmonic after cooling again is less than the initial value.

Beside the described aspects some more features of the phase transition can be extracted from this measurements. One can see that there is a peak around the phase transition in both heating curves. This feature is at lower temperature for the forward SHG than the one recorded at 90°. The origin of this peak must be connected with the phase transition of the crystal. When the temperature of the crystal is in the Curie region then the monodomain sample will start to break into smaller domains. Also parts of the crystal jump

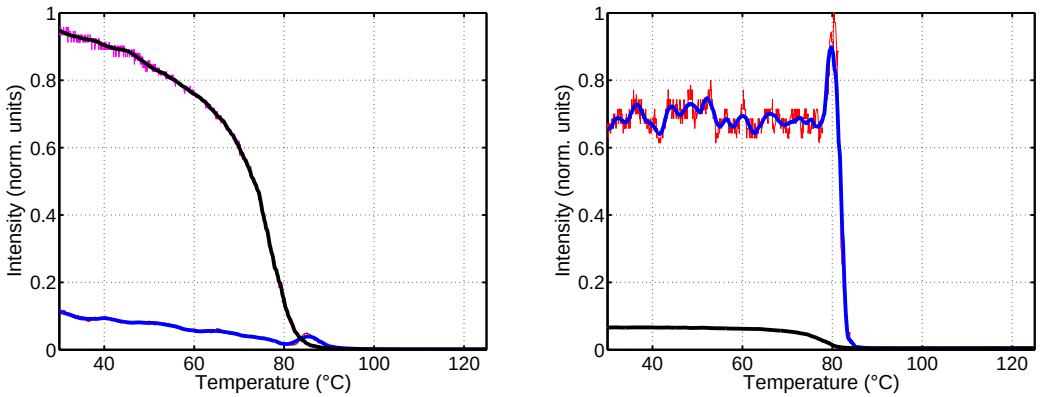

Figure 6.5: SHG measurements on a poled, congruently melting SBN crystal. The data on the left are measured with a photomultiplier recording the signal under an angle of 90° regarding the direction of the laser beam. The lower curve is for the heating and the upper one is for cooling of the sample. The right graphs are forward SHG. The upper curve represents the heating and the lower one the cooling of the crystal.

to the paraelectric phase. As a first result of this fact an inhomogeneity of the refractive index will appear in the sample and this may lead to a pronounced scattering of the SHG. The fact that this peak is found at lower temperature for the forward multiplier is not accidental. The initial state of the sample is mono-domain thus small $\mathbf{K}_g$ vectors will prevail. At the moment when very large domains break this peak is seen at the 0° photomultiplier. After this no longer large domains or in other words no longer small $\mathbf{K}_g$ vectors are present. This can be clearly observed in the steep decrease of the SHG intensity, in forward direction, after the peak. Concomitantly with the breakup of the mono-domain *(or of the very large domains)* several smaller ferroelectric domains will be generated. That means the density of the larger $\mathbf{K}_g$ vectors will increase and thus the intensity of the SHG measured at 90° will be enhanced. With increasing temperature also the smaller ferroelectric domains will transform into the paraelectric phase and finally the intensity of the second harmonic will be depleted all around the crystal.

The peak seen in forward direction is not perfectly reproducible. Even for the same sample after two consecutive measurements, with the crystal in the same initial state and with all the measurement parameters unchanged the intensity of the peak can largely vary from a relative pronounced shape to practically no intensity. This is connected with the explained origin of the peak. It is important to underline that the peak recorded at 0° has approximately the same width for all compositions of the crystal from the most Strontium rich to the most Barium rich. And the peak can more often be seen for the Strontium rich composition. Also different heating-speeds *(in the region from 5°C/hour to 200°C/hour)* can not affect any properties of this feature.

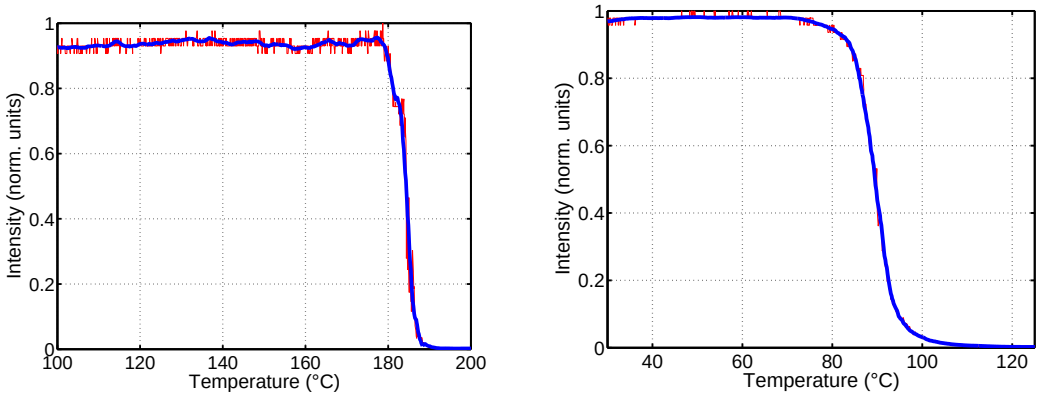

Figure 6.6: Comparison between the phase transition of a sample with high Barium content *left* and the phase transition of the congruently melting composition *right*. The Barium rich composition ($x = 0.41$) has a much smaller Curie region than the congruent one.

On the other hand the peak recorded at 90° is strongly depending on the Strontium - Barium ratio. In the case of a high Strontium content the peak is broad and is expanded over the hole Curie region. The peak height is depending on the poling history, if the poling was made at a higher voltage then also the peak is higher.
The width is independent of the poling voltage, is also independent of heating speed during the measurement. For the crystals with a high Barium content this feature is difficult to be seen and for the values of $x < 0.48$ the peak is no longer present. As it was described, in this region the crystal is the most homogeneous. Also the phase transition shows only very slight relaxor features. As can be observed in Fig. 6.6 the phase transition can nearly be described with a delta function. Several authors in the literature are talking about a 'close first' order phase transition of the material for this composition region [19, 62, 64]. Dielectric constant measurements show, however, that this can not be regarded as first order phase transition but the Curie region is extremely small. Thus one can assume that all processes in the crystal are very fast during the phase transition and no meta-stable states can be experimentally seen.

The pinning effect, observed in hysteresis measurements [22, 23, 70, 71], leads also to a redistribution of the $\mathbf{K}_g$ vectors in the same manner as the high temperature poling does. To investigate this, high voltage cycles were applied on SBN crystals of different compositions. For electric fields over 600 V/mm the density of small $\mathbf{K}_g$ vectors increases and for large vectors decreases. All happens just after the first cycle. Further cycling of the sample does not bring any new results. Figure 6.8 shows a typical cycling measurement in the case of the congruently melting composition. Five complete cycling loops were made, the SHG intensity is practically constant after the first cycle. Similar results are found for all crystals at temperatures well below the phase transition.

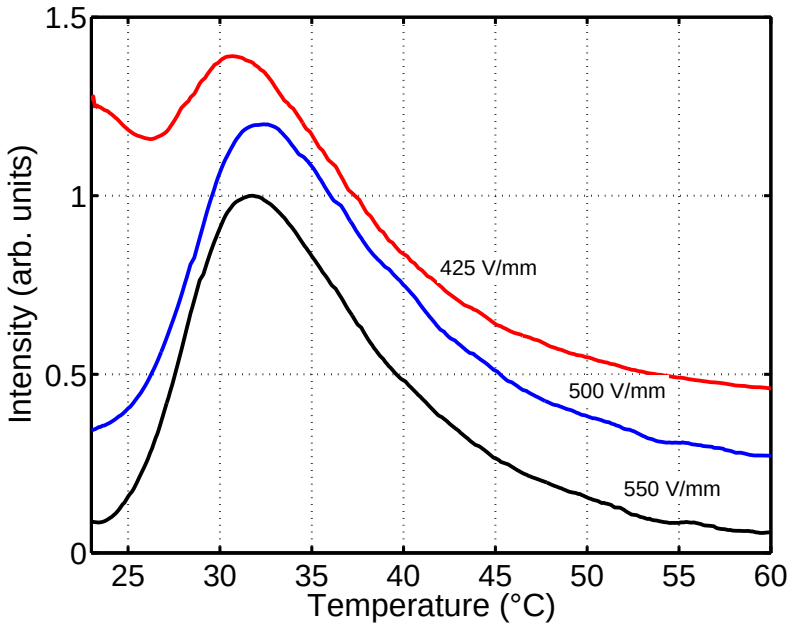

Figure 6.7: SHG peak intensity of a sample with composition $x = 0.74$ recorded at 90° with respect to the direction of the infrared beam. The difference between the curves is the poling voltage of the sample. One can observe that the higher the voltage the more expressed the peak is.

As shown in Chapter 5.2, from the divergence of the SHG light it is possible to evaluate the minimum domain length. Because of the finite length of the ferroelectric domains a larger than zero grating vector component in the c-direction can contribute to the momentum conservation. Thus the generated second harmonic light has a certain divergence in this direction. By a careful measurement of the light divergence it was determined that the shortest domains have a length around 20 μm independent of the Strontium - Barium ratio. This length of the shortest domains could not be increased by poling. We verified this by applying voltages up to the breakdown of the samples. From this we must conclude that even in nominally single domain samples substructures of this typical size exist. This seems to be particularly true for undoped SBN. For doped samples the situation might be different. A preliminary measurement on one doped sample available (1200 ppm Cerium, congruently melting composition) revealed that there the length of the domains can be increased by poling and even by room temperature cycling. Authors like Granzow et al. [58] report an increase of the phase transition temperature after the sample was poled. With our samples it was not possible to see this increase but it is very likely that this is the case especially for highly doped crystals. At least two facts favor this assumption. The domain length is changed by poling, and -due to a lower electrical conductivity- higher fields can be applied on the samples during the poling procedure compared to the situation in the undoped crystal.

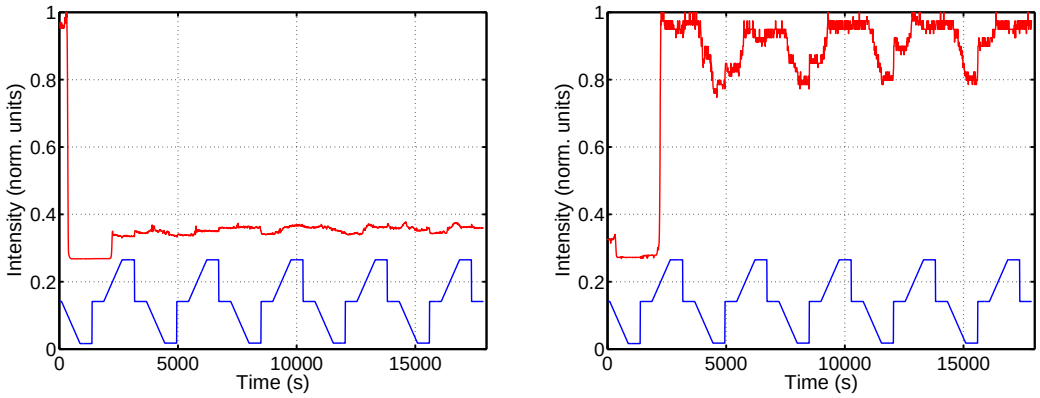

Figure 6.8: Room temperature cycling of a congruently melting composition SBN crystal. The *left* image was recorded perpendicular to the direction of the laser beam. The lower curve shows the applied voltage, the above curve is the measured SHG intensity. The *right* curve presents the same as the left one but for the forward direction. One can see that the SHG light intensity is enhanced in forward direction and decreased for 90°. The cycling was made between ±600 V/mm.

Chapter 7

Conclusion

Let us briefly summarize the material presented in the preceding chapters:

- Refractive index measurements of the Strontium-Barium-Niobate (SBN) crystals show that none of the known second-harmonic-generation scheme (SHG) can be hold responsible for the SHG in SBN.
- Based on observations of the SHG experiments carried out with several compositions of the crystals in different setup-geometries a new model of second harmonic generation was developed.
- The new SHG model, domain-induced-second-harmonic-generation (DISHG), which considers that the needle-like domain structure of this material plays an active role in the quasi phase matching of the produced second harmonic light have been experimentally proved using two different experiments.
- The new SHG process in the SBN crystals is a potential light source of cylindrically polarized light. Several theoretical studies have shown that the cylindrical, highly symmetric, light polarization state is an advantage in the light focusing. The focusing diameter is smaller for such a light polarization than for any other. The easy way of obtaining a cylindrically polarized light with the SBN crystal broaden the potential applications for this material.
- The (DISHG) allowed us to investigate several properties of the ferroelectric domains. Using SHG measurements it was possible to analyze the development of the domain densities for domains of different sizes during the poling of the crystal.
- SHG measurements allow us to determine the minimum length of the ferroelectric domains. It was shown that this dose not depend on the [Sr]/[Ba] ratio and domains are not getting longer after the sample was poled, except for the case of doped SBN.
- The ferroelectric-paraelectric phase transition has also been investigated. From the inflection point of the nonlinear susceptibility as function of the temperature the

phase transition temperature was determined. The non fully-linear dependence of the phase transition temperature as function of the [Sr]/[Ba] ratio can be explained by a system of three different sublattices at the crystallographic positions of Strontium and Barium atoms.

- Measurements in the Strontium rich compositions showed an important compositional inhomogeneity of the material which can be the main reason for the pronounced relaxor behavior. Scattering effects of the second harmonic light due to refractive index inhomogeneities near the phase transition revealed that in this composition region the crystal dose not undergo the phase transition in the whole bulk at the same temperature.

On the basis of this thesis, further research should be carried out in several directions:

- Focusing experiments with cylindrically polarized light should manifest the theoretical prediction of the focusing behavior of such light.
- Using DISHG, the domain behavior in doped SBN can be investigated.
- A three-dimensional composition topography of SBN will be facilitated by an extremely focused fundamental beam.
- Further investigations should be carried out for a better understanding of the ferroelectric-paraelectric phase transition in SBN.
- DISHG may be investigated in different crystals -similar in structure like e.g. Barium Strontium Niobate- too.

Bibliography

[1] A. M. Glass. Investigation of the electrical properties of $Ba_xSr_{1-x}Nb_2O_6$ with special reference to pyroelectric detection. *J. App. Phys.*, 40:4699, 1969.

[2] F. Kahmann, J. Hohne, R. Pankrath, and R. A. Rupp. Hologram recording with mutually orthogonal polarized waves in $Sr_{0.61}Ba_{0.39}Nb_2O_6$:Ce. *Phys. Rev. B*, 50:2474, 1994.

[3] P. B. Jamieson, S. C. Abrahams, and J. L. Bernstein. Ferroelectric Tungsten Bronze-Type Crystal Structures. I. Barium Strontium Niobate $Ba_{0.27}Sr_{0.75}Nb_2O_{5.78}$. *J. Chem. Phys.*, 48:5048, 1968.

[4] A. E. Andreichuk, L. M. Dorozhkin, Yu. S. Kuzminow, I. A. Maslyanitsun, V. N. Molchanov, A. A. Rusakov, V. I. Simonov, V. D. Shigorin, and G. P. Shipulo. Quadratic optical susceptibility and structure of $Ba_xSr_{1-x}Nb_2O_6$ crystals. *Sov. Phys. Cryst.*, 29:641, 1984.

[5] T. S. Chernaya, B. A. Maksimov, I. V. Verin, L. I. Ivleva, and V. I. Simonov. Crystal structure of $Ba_{0.39}Sr_{0.61}Nb_2O_6$ single crystals. *Cryst. Rep.*, 42:375, 1997.

[6] M. P. Trubelja, E. Ryba, and D. K. Smith. A study of positional disorder in strontium barium niobate. *J. Mat. Sci.*, 31:1435, 1996.

[7] A. Tunyagi, M. Ulex, and K. Betzler. Non-collinear optical frequency doubling in strontium barium niobate. *Phys. Rev. Lett.*, 90:243901, 2003.

[8] S. Quabis, R. Dorn, M. Eberler, O. Glöckl, and G. Leuchs. Focusing light to a tighter spot. *Opt. Commun.*, 179:1, 2000.

[9] S. Quabis, R. Dorn, M. Eberler, O. Glöckl, and G. Leuchs. Focusing light - theoretical calculation and experimental tomographic reconstruction. *App. Phys. B*, 72:109, 2001.

[10] S. Quabis, R. Dorn, M. Eberler, O. Glöckl, and G. Leuchs. Reduction of the spot size by using a radially polarized laser beam. *Proc. SPIE*, 4429:105, 2000.

[11] Z. Bomzon, V. Kleiner, and E. Hasman. Formation of radially and azimuthally polarized light using space-variant subwavelength metal stripe gratings. *App. Phys. Lett.*, 79:11, 2001.

[12] R. Dorn, S. Quabis, and G. Leuchs. The focus of light - linear polarization breaks rotational symmetry of the focal spot. *App. Phys. Lett.*, 50:1917, 2003.

[13] A. Tunyagi and K. Betzler. Lichtquelle für radial polarisiertes Licht. *Patent Application.*, page 10 2004 013 284.4, 2004.

[14] R. R. Neurgaonkar, M. H. Kalisher, T. C. Lim, E. J. Staples, and K. L. Kester. Czochralski single crystal growth of SBN:61 for surface acoustic wave applications. *Mater. Res. Bulletin.*, 15:1235, 1980.

[15] H. Y. Zhang, X. H. He, Y. H. Shih, and L. Yan. Picosecond phase conjugation and 2-wave coupling in strontium barium niobate. *J. Mod. Opt.*, 41:669, 1994.

[16] M. Wesner, C. Herden, R. Pankrath, D. Kip, and P. Moretti. Temporal development of photorefractive solitons up to telecommunication wavelengths in strontium-barium niobate waveguides. *Phys. Rev. E*, 6403:6613, 2001.

[17] A. S. Kewitsch, M. Segev, A. Yariv, G. J. Salamo, T. W. Towe, E. J. Sharp, and R. R. Neurgaonkar. Tunable quasi-phase matching using dynamic ferroelectric domain gratings induced by photorefractive space-charge fields. *App. Phys. Lett.*, 64:3068, 1994.

[18] R. R. Neurgaonkar, W. K. Cory, J. R. Oliver, E. J. Sharp, M. J. Miller, G. L. Wood, W. W. Clark, A. G. Mott, G. J. Salamo, and B. D. Monson. Photorefractive tungsten bronze materials and applications. *SPIE.*, 2:1148, 1989.

[19] L. E. Cross. Relaxor ferroelectrics. *Ferroel.*, 76:241, 1987.

[20] J. R. Oliver, R. R. Neurgaonkar, and L. E. Cross. A thermodynamic phenomenology for ferroelectric tungsten bronze $Sr_{0.6}Ba_{0.4}Nb_2O_6$ (SBN:60). *J. Appl. Phys.*, 64:37, 1988.

[21] M. Ulex, R. Pankrath, and K. Betzler. Growth of strontium barium niobate: The liquidus-solidus phase diagram. *J. Cryst. Growth, in press*, 2004.

[22] W. H. Huang, Z. Xu, and D. Viehland. Structure-property relationships in strontium barium niobate II. *Philos. Mag.*, 71:219, 1995.

[23] W. H. Huang, Z. Xu, and D. Viehland. Structure-property relationships in strontium barium niobate I. *Philos. Mag.*, 71:205, 1995.

[24] T. S. Chernaya, B. A. Maksimov, T. R. Volk, L. I. Ivleva, and V. I. Simonov. Atomic structure of $Sr_{0.75}Ba_{0.25}Nb_2O_6$ single crystal and composition-structure-property relation in (Sr,Ba)Nb_2O_6 solid solutions. *Phys. Sol. State*, 42:1716, 2000.

[25] N. Blombergen. *Nonlinear Optics*. W. A. Benjamin, New York, 1965.

[26] P. Hertel. *Linear Response Theory*. Lecture University of Osnabrueck, Osnabrueck, 2001.

[27] M Wöhlecke, K. Betzler, and M. Imlau. *Nonlinear Optics*. Lecture University of Osnabrueck, Osnabrueck, 2003.

[28] R. Menzel. *Linear and Nonlinear Interactions of Laser Light and Matter*. Springer, Springer - Verlag Berlin Heidelberg New York, 2001.

[29] D. A. Kleinman. Nonlinear dielectric polarization in optical media. *Phys. Rev.*, 126:1977, 1962.

[30] Y. R. Shen. *The Principles of Nonlinear Optics*. Wiley, New York, 1984.

[31] P. A. Franken, A. E. Hill, C. W. Peters, and G. Weinreich. Generation of optical harmonics. *Phys. Rev. Lett.*, 7:118, 1961.

[32] T. H. Maiman. Stimulated optical radiation in ruby. *Nature*, 187:493, 1960.

[33] J. A. Armstrong, N. Bloembergen, J. Ducuing, and P. S. Pershan. Interactions between light waves in a nonlinear dielectric. *Phys. Rev.*, 127:1918, 1962.

[34] V. Ya. Shur, E. L. Rumyantsev, E. V. Nikolaeva, E. I. Shishkin, R. G. Batchko, M. M. Fejer, and R. L. Byer. Recent achievements in domain engineering in lithium niobate and lithium tantalate. *Ferroel.*, 257:191, 2001.

[35] M. M. Fejer, G. A. Magel, D. H. Jundt, and R. L. Byer. Quasi-phase-matched second harmonic generation tuning and tolerances. *IEEE J. Quant. Elect.*, QE-28:2631, 1992.

[36] M. Fox. *Optical Properties of Solids*. Oxford University Press, Oxford University Press Inc. - New York, 2001.

[37] U. Schlarb and K. Betzler. Influence of the defect structure on the refractive indices of undoped and Mg - doped lithium niobate. *Phys. Rev. B*, 50:751, 1994.

[38] U. Schlarb and K. Betzler. A generalized Sellmeier equation for the refractive indices of lithium niobate. *Ferroel.*, 99:156, 1994.

[39] A. Reichert and K. Betzler. Induced noncolinear frequency doubling a new characterization technique for electrooptic crystals. *J. Appl. Phys.*, 79:2209, 1996.

[40] K. U. Kasemir and K. Betzler. Characterization of photorefractive materials by spontaneous noncolinear frequency doubling. *App. Phys. B*, 68:763, 1999.

[41] K. D. Moll, D. Homoelle, Alexander L. Gaeta, and Robert W. Boyd. Conical harmonic generation in isotropic materials. *Phys. Rev. Lett.*, 88:153901, 2002.

[42] F. L. Venturini, E. G. Spencer, P. V. Lenzo, and A. A. Ballman. Refractive indices of strontium barium niobate. *J. App. Phys.*, 39:343, 1968.

[43] D. Kip, S. Aulkemeyer, K. Buse, F. Mersch, R. Pankrath, and E. Kratzig. Refractive indices of $Sr_{0.61}Ba_{0.39}Nb_2O_6$ single crystals. *Phys. Stat. Sol. A*, 154:5, 1996.

[44] T. Woike, T. Granzow, U. Dörfler, C. Poetsch, M. Wöhlecke, and R. Pankrath. Refractive indices of congruently melting $Sr_{0.61}Ba_{0.39}Nb_2O_6$. *Phys. Stat. Sol. A*, 186:13, 2001.

[45] M. Esser, M. Burianek, P. Held, J. Stade, S. Bulut, C. Wickleder, and M. Mühlberg. Optical characterization and crystal structure of the novel bronze type $Ca_xBa_{1-x}Nb_2O_6$ (x = 0.28; CBN - 28). *Crys. Res. Technol.*, 6:457, 2003.

[46] S. Singh, D. A. Draegert, and J. E. Geusic. Optical and ferroelectric properties of barium sodium niobate. *Phys. Rev. B.*, 2:2709, 1970.

[47] B. Sturman, S. G. Odoulov, and M. Yu. Goulkov. The growth and properties of SBN, a tungsten bronze ferroelectric. *Phys. Rep.*, 275:199, 1996.

[48] L. Solymar, D. J. Webb, and A. Grunnet-Jepsen. *The Physics and Applications of Photorefractive Materials*. Clarendon Press, Oxford, 1996.

[49] M. Goulkov, S. Odoulov, I. Naumova, F. Agulló-López, G. Calvo, E. Podivilov, B. Sturman, and V. Pruneri. Degenerate parametric light scattering in periodically poled $LiNbO_3$:Y:Fe. *Phys. Rev. Letters*, 86:4021, 2001.

[50] S. Kawai, T. Ogawa, H. S. Lee, Robert C. DeMattei, and Robert S. Feigelson. Second-harmonic generation from needlelike ferroelectric domains in $Sr_{0.6}Ba_{0.4}Nd_2O_6$ single crystals. *Appl. Phys. Lett.*, 73:768, 1998.

[51] Y. G. Wang, W. Kleemann, Th. Woike, and R. Pankrath. Atomic force microscopy of domains and volume holograms in $Sr_{0.61}Ba_{0.39}Nd_2O_6$:$Ce^{3+}$. *Phys. Rev. B*, 6133:330, 2000.

[52] W. Kleemann, P. Licinio, Th. Woike, and R. Pankrath. Dynamic light scattering at domains and nanoclusters in a relaxor ferroelectric. *Phys. Rev. Lett.*, 86:6014, 2001.

[53] P. Lehnen, W. Kleemann, Th. Woike, and R. Pankrath. Ferroelectric nanodomains in the uniaxial relaxor system $Sr_{0.61-x}Ba_{0.39}Nd_2O_6$:$Ce^{3+}_x$. *Phys. Rev. B*, 6422:4109, 2001.

[54] P. Lehnen, W. Kleemann, Th. Woike, and R. Pankrath. Phase transitions in $Sr_{0.61}Ba_{0.39}Nb_2O_6$:$Ce^{3+}$: II. linear birefringence studies of spontaneous and precursor polarization. *Euro. Phys. Jour. B*, 14:633, 2000.

[55] R. R. Neurgaonkar, W. K. Cory, and J. R. Oliver. Growth and optical pproperties of ferroelectric tungsten bronze crystals. *Ferroel.*, 142:167, 1993.

[56] L. E. Cross and D. Viehland. Piezoelectricity in tungsten bronze crystals. *Ferroel.*, 160:265, 1994.

[57] P. B. Jamieson, S. C. Abrahams, and J. L. Bernstein. Ferroelectric Tungsten Bronze-type Crystal Structures. II Barium Sodium Niobate $Ba_xSr_{1-x}Nb_2O_6$. *J. Chem. Phys.*, 50:4352, 1969.

[58] T. Granzow, U. Dörfler, T. Woike, M. Wöhlecke, R. Pankrath, M. Imlau, and W. Kleemann. Evidence of random electric fields in the relaxor-ferroelectric $Sr_{0.61}Ba_{0.39}Nb_2O_6$. *Euro. Phys. Lett.*, 57:597, 2002.

[59] W. Kleemann, J. Dec, R. Blinc, B. Zalar, and R. Pankrath. Random fields at transitions from relaxor to glassy and ferroelectric states. *Ferroel.*, 267:157, 2002.

[60] W. Kleemann. Random fields in dipolar glasses and relaxors. *J. of Non-Cryst. Sol.*, 307:66, 2002.

[61] J. Dec, W. Kleemann, T. Woike, and R. Pankrath. Phase transition in SBN:Ce susceptibility of cousters and domains. *Eur. Phys. J. B*, 14:627–632, 2000.

[62] A. F. Devonshire. Theory of ferroelectrics. *Phil. Mag.*, 3:85, 1954.

[63] C. David, T. Granzow, A. Tunyagi, M. Wöhlecke, Th. Woike, K. Betzler, M. Ulex, M. Imlau, and R. Pankrath. Composition dependence of the phase transition temperature in $Sr_xBa_{1-x}Nb_2O_6$. *Phys. Stat. Sol.*, 8:49, 2004.

[64] I. A. Santos and J. A. Eiras. Phenomenological description of the diffuse phase transition in ferroelectrics. *Journal of Physics-Condensed Matter*, 13:11733, 2001.

[65] M. E. Lines and A. M. Glass. *Principles and Applications of Ferroelectrics and Related Materials*. Clarendon Press Oxford, Oxford, 1977.

[66] G. A. Smolenskij, V. A. Isupov, A. I. Agranovskaya, and S. N. Popov. Composition dependence of the phase transition temperature in $Ba_xSr_{1-x}Nb_2O_6$. *Sov. Phys. Solid State*, 2:2584, 1961.

[67] T. S. Chernaya, B. A. Maksimov, I. A. Verin, L. I. Ivleva, and V. I. Simonov. Refinement of the single-crystal structure of $Sr_xBa_{1-x}Nb_2O_6$. *Cryst. Rep.*, 43:986, 1998.

[68] J. A. Gonzalo. *Effective Field Approach to Phase Transitions and Some Applications to Ferroelectrics*. World Scientific Press, Singapore, 1991.

[69] R. A. Ali, C. L. Wang, M. Yuan, Y. X. Wang, and W. L. Zhong. Compositional dependence of the curie temperature in mixed ferroelectrics: effective field approach. *Sol. St. Commun.*, 129:365, 2004.

[70] T. Granzow, U. Dörfler, T. Woike, M. Wöhlecke, R. Pankrath, M. Imlau, and W. Kleemann. Influence of pinning effects on the ferroelectric hysteresis in cerium-doped $Sr_{0.61}Ba_{0.39}Nb_2O_6$ - art. no. 174101. *Phys. Rev. B*, 6317:4101, 2001.

[71] T. Woike, T. Volk, U. Dörfler, R. Pankrath, L. Ivleva, and M. Wöhlecke. Ferroelectric and optical hysteresis in sbn doped with rare earth elements. *Ferroel. Lett.*, 23:127, 1998.

Acknowledgements

I consider myself to be a lucky person, since I have met a lot of good people who have supported my way to this thesis.

I am especially thankful to apl. Prof. Dr. Klaus Betzler. This thesis would be simply impossible without his overall help and support. The support and help of Prof. Betzler were not limited to the scientific supervision, but have extended to many problems of a daily life.

I would like to thank apl. Prof. Dr. Manfred Wöhlecke for friendly encouragements and useful discussions regarding scientific problems, also for his help with several occasions when accommodation difficulties arises.

I thank Dr. Rainer Pankrath and Dr. Michael Ulex for the growth SBN crystals which were the base materials for this work.

I thank Dr. Tania Volk for useful advice and fruitful discussions regarding scientific problems connected with this work.

I am also grateful to Mrs. Gerda Cornelsen, Mr. Gregor Steinhoff and Dr. Wolfgang Mikosch for many helps with several occasions during my stay at Osnabrueck University.

The financial support from the Graduate College *Nonlinearities of Optical Materials*, financed by the Deutsche Forschungsgemeinschaft and the Federal State of Niedersachsen, is gratefully acknowledged.